Contrail Modeling and Simulation

Roberto Paoli[1,*] and Karim Shariff[2]

[1]CERFACS, 31057 Toulouse Cedex 01, France; email: paoli@cerfacs.fr

[2]NASA Ames Research Center, Moffett Field, California 94035; email: karim.shariff@nasa.gov

Annu. Rev. Fluid Mech. 2016. 48:393–427

The *Annual Review of Fluid Mechanics* is online at fluid.annualreviews.org

This article's doi: 10.1146/annurev-fluid-010814-013619

*Current affiliations: Department of Mechanical and Industrial Engineering, University of Illinois at Chicago, Illinois 60607 and Argonne National Laboratory, Argonne, Illinois 60439

Keywords

two-phase flow, particulate flows, vortex dynamics, stratified flow, cloud formation and dynamics, large-eddy simulation, radiative hydrodynamics

Abstract

There is large uncertainty in the radiative forcing induced by aircraft contrails, particularly after they transform to cirrus. It has recently become possible to simulate contrail evolution for long periods after their formation. We review the main physical processes and simulation efforts in the four phases of contrail evolution, namely the jet, vortex, vortex dissipation, and diffusion phases. Recommendations for further work are given.

1. INTRODUCTION

1.1. Context and Motivation

UTLS: upper troposphere/lower stratosphere

IPCC: Intergovernmental Panel of Climate Change

RF: radiative forcing

Commercial aircraft engines emit hot gases and particulates consisting of carbon dioxide (CO_2), water vapor (H_2O), nitrogen oxide (NO_x), sulfur oxide (SO_x), hydrocarbon (HC), and soot particles (**Figure 1**). Because of long residence times and low background concentrations, aircraft emissions affect the chemical composition of the upper troposphere/lower stratosphere (UTLS), altitudes between 9 and 12 km, where the largest time is spent in long-haul flights. The Earth's radiation budget is particularly sensitive to temperature and composition changes in the UTLS (Riese et al. 2012). For sufficiently low ambient temperature, aircraft emissions also increase the Earth's cloudiness by triggering the formation of condensation trails (contrails), line-shaped ice clouds that are visible behind aircraft (Schumann 1996, 2005). Contrails can spread under conditions of high ambient humidity and evolve into contrail cirrus that can last for a few hours, becoming indistinguishable from natural cirrus when viewed by satellite instruments (Minnis et al. 1998).

Commercial air traffic is expected to grow at an average yearly rate of 5–7% over the period 2005–2025 (Int. Civil Aviat. Organ. 2007, Wilkerson et al. 2010). Therefore, the environmental and climatic impact of aircraft emissions is becoming a source of increasing concern among scientists and policy makers (Lee et al. 2009, 2010). In 1999, the Intergovernmental Panel of Climate Change (IPCC) provided the first comprehensive assessment of aviation's impact on climate in terms of the radiative forcing (RF) induced by aircraft emissions (Penner et al. 1999, Prather et al. 1999). RF is a measure of the perturbation of the atmospheric energy budget and is defined as the net change, $\Delta F \equiv \mathrm{RF}$, in radiative flux resulting from changes in the atmospheric composition relative to a reference state (Shine et al. 1990) (see **Figure 2**). It is widely used as a climate metric (Fuglestvedt et al. 2003, Sausen et al. 2005). According to Lee et al. (2009), aviation's contribution to anthropogenic RF is 2–14% (90% likelihood range). After a particular forcing is applied, a certain change ΔT_s in the mean surface temperature will result when equilibrium is reached. The ratio of ΔT_s to RF is referred to as the climate sensitivity λ (Cess et al. 1990):

$$\Delta T_s \equiv \lambda\, \mathrm{RF}. \tag{1}$$

We note that different forcing mechanisms can have very different climate sensitivities.

IPCC estimates were re-evaluated in 2005, with new observational data and modeling studies (Sausen et al. 2005, Lee et al. 2009); they are summarized in **Figure 3**. The main point to note

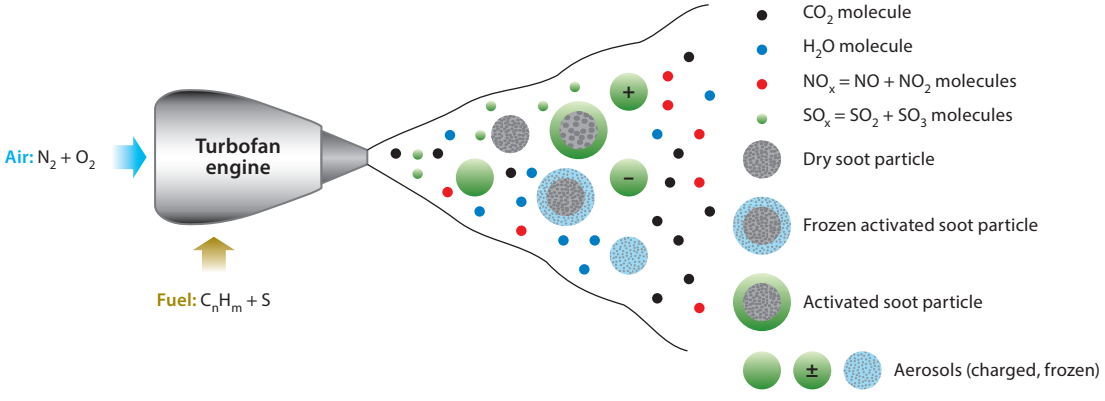

Figure 1

The principal gaseous and particulate exhausts from modern turbofan engines.

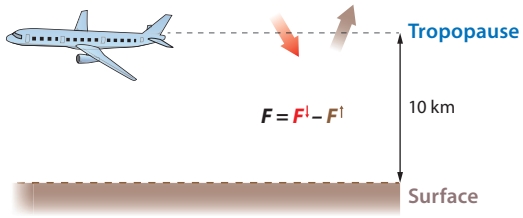

Figure 2

Diagram of the net radiative energy flux (net irradiance) defined as the difference between the incoming solar energy flux $F^{\downarrow}$ (*red*) and the outgoing energy flux $F^{\uparrow}$ (*brown*) reflected back to space by the Earth at the tropopause level (top of the atmosphere): $F = F^{\downarrow} - F^{\uparrow}$.

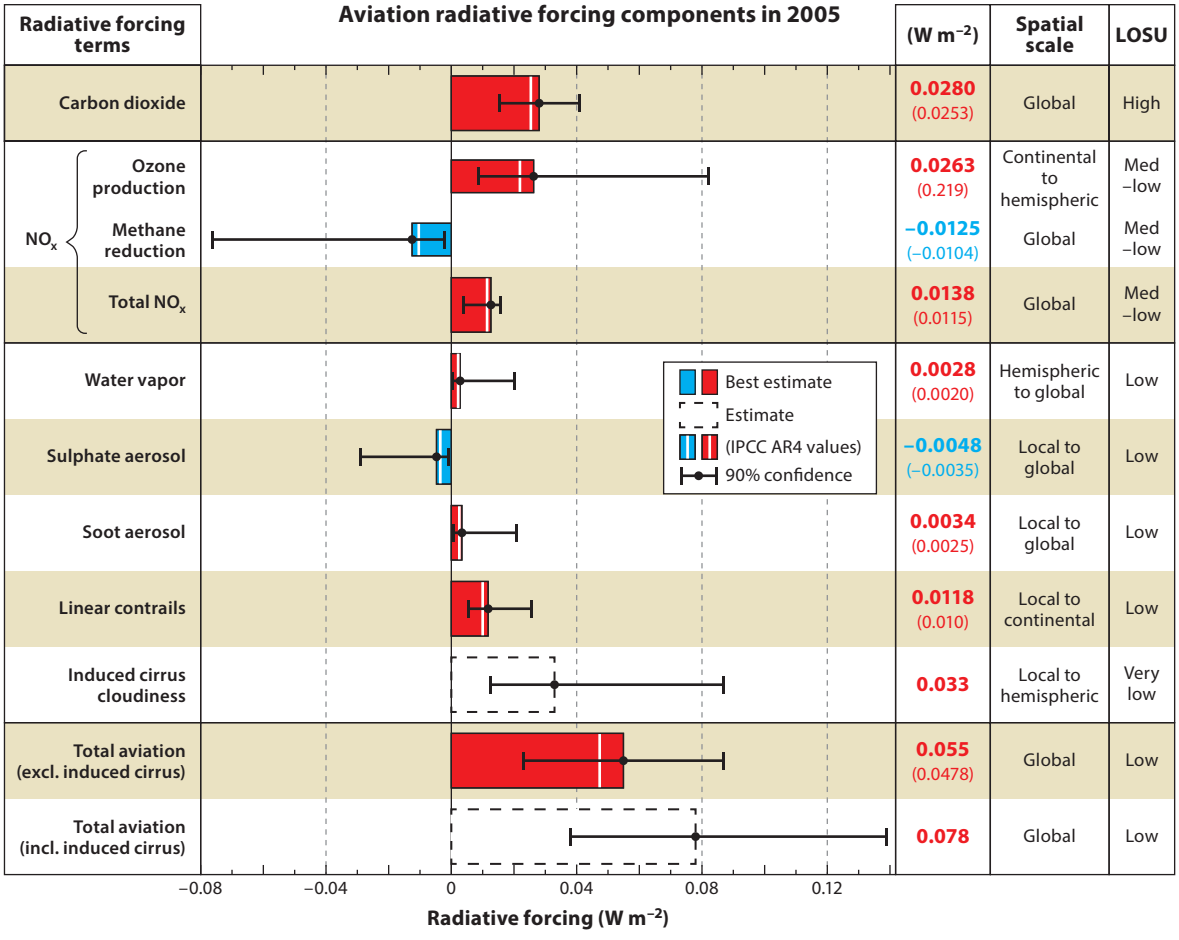

Figure 3

Radiative forcing from global aviation emissions (Sausen et al. 2005, Lee et al. 2009). Figure adapted with permission from Lee et al. (2009). Abbreviations: IPCC, Intergovernmental Panel of Climate Change; LOSU, level of scientific understanding.

is that the effect of induced cirrus is given as an estimate with an uncertainty range larger than the sum of all other sources. Induced cirrus has two contributions: contrails transforming into cirrus (see Section 5) and artificial cloud condensation nuclei promoting cirrus. The RF of linear contrails, which are conceptually simpler, also has significant uncertainty. These uncertainties have motivated intense modeling, computational, experimental, and observational work on contrails over the past two decades. For example, the European Commission and the Federal Aviation Administration have supported large-scale initiatives in this area, such as the projects QUANTIFY (2005–2010) and ACCRI (2010–2014), respectively. In the framework of ACCRI, a series of white papers presented the current status of knowledge of contrail microphysics (Heymsfield et al. 2010), optics and radiation (Yang et al. 2010), and global modeling (Burkhardt et al. 2010).

1.2. Summary of the Regimes of Evolution

Predicting the RF of aircraft-induced cloudiness presents two types of difficulties. The first pertains to resolving and predicting the UTLS environment. This includes ice supersaturated regions, which can exist at many horizontal length scales and thin vertical scales (Gierens & Spichtinger 2000, Lamquin et al. 2012), as well as stably stratified turbulence, which consists of inertial-gravity waves and vertically layered structures. The second class of issues, which are the main concern of this review, involves modeling all the fluid dynamical and physicochemical processes that drive the transformations of contrails in the aircraft wake and in the free atmosphere (Lee et al. 2009). The overarching goal of research in this field is to perform simulations of increasing fidelity to identify the most important processes and then to use the results to build simpler parameterizations that can be incorporated into general circulation models, which typically have grid sizes of a few hundred kilometers for simulations that cover the entire globe (Burkhardt & Kärcher 2009, Jacobson et al. 2011, Schumann 2012).

For convenience, contrail evolution is divided into four regimes (Gerz et al. 1998) (**Figure 4**). First, in the first few seconds after emission (the jet regime), the vortex sheet shed by the wings rolls up into a pair of counter-rotating vortices (called the primary wake), while freshly nucleated ice crystals in the engine exhaust are trapped around the cores of these vortices. Second, in the minutes following the first phase (the vortex regime), the vortices descend in the atmosphere because of their mutually induced downward velocity. Vortex descent creates a density contrast between the air carried with the vortices (in an oval-shaped region) and the ambient air. This results in the creation of vorticity of opposite sign (in a stably stratified atmosphere) on the oval boundary. Shedding of this vorticity upward forms a secondary wake, and part of the exhaust and ice particles is detrained into the secondary wake. The portion of the exhaust trapped in the primary wake participates with the wake in complex vortex instability processes. Third, in the vortex-dissipation regime, the primary vortex pair and secondary vorticity disintegrate and dissipate, releasing exhaust and ice crystals, which eventually sublimate. Ice crystals released in the secondary wake can persist longer because of the lower temperature. Finally, during the diffusion regime, atmospheric turbulence, particle sedimentation, radiative processes, and wind shear control the horizontal and vertical spreading of the contrail until complete mixing occurs, usually within a few hours.

1.3. Scope

This review describes recent work and current trends in the modeling and simulation of contrails in the four regimes described above. We focus on the interaction between fluid mechanics and

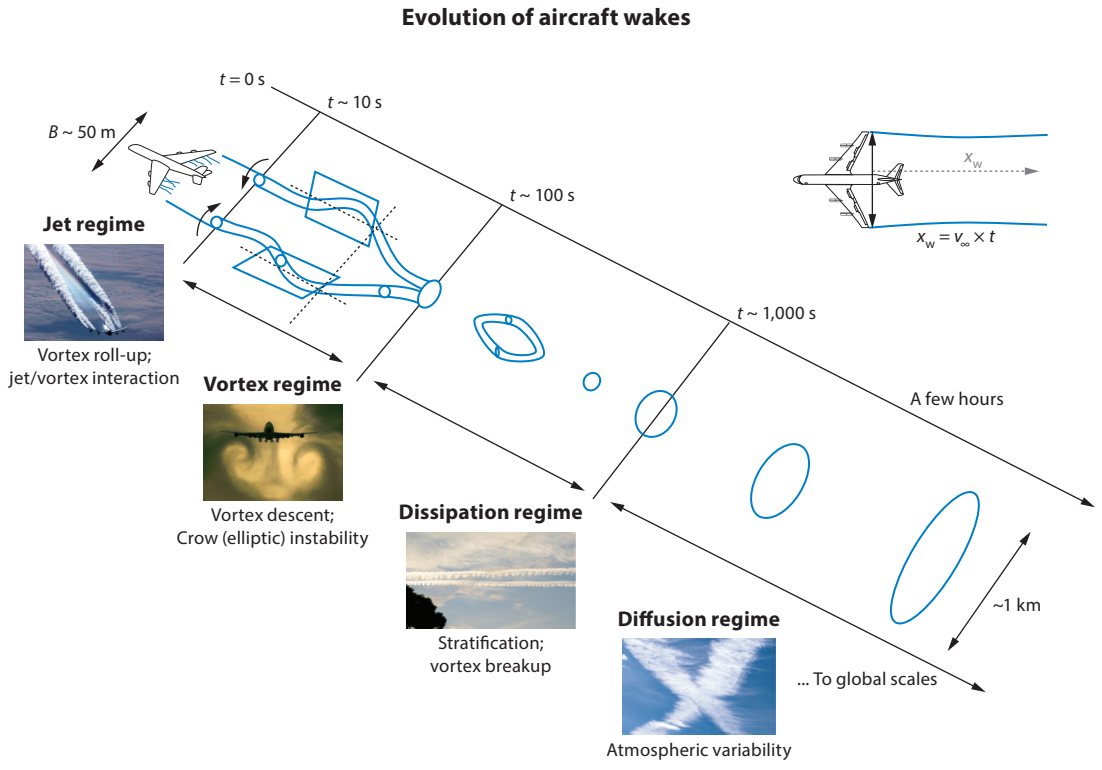

Figure 4

Classification of aircraft wake evolution into four regimes (Gerz et al. 1998) following a tracer exhaust emitted at $t = 0$ from the nozzle exit. The wake distance behind the aircraft is $x_w = v_\infty t$, where v_∞ is the aircraft speed.

microphysics and on computational approaches such as large-eddy simulation (LES) that allow one to explicitly solve for contrail structure.

2. PHYSICS

2.1. Formation Criterion

According to the Schmidt-Appleman criterion (Schmidt 1941, Appleman 1953), contrail formation is explained by the increase in relative humidity that occurs in the jet plume as moist but unsaturated hot exhaust gases mix with cold ambient air. The mixing process can be conveniently illustrated in a thermodynamic diagram that plots the water vapor partial pressure $P_v \equiv X_{H_2O} P$ (where X_{H_2O} is the vapor mole fraction) as a function of temperature T (**Figure 5**). Assuming that the process is adiabatic and vapor conserving, and that vapor and heat diffuse at the same rate, we can represent mixing by a straight line connecting the points corresponding to engine exit conditions $\{T_j; P_{v_j}\}$ and ambient conditions $\{T_\infty; P_{v_\infty}\}$. The slope G of the mixing line can be expressed in terms of atmospheric conditions and the propulsive characteristics of the engine (Schumann 1996, his equation 8):

$$G \equiv \frac{P_{v_j} - P_{v_\infty}}{T_j - T_\infty} = \frac{c_p P_\infty \mathrm{EI}_{H_2O}}{\varepsilon Q(1-\eta)}, \qquad (2)$$

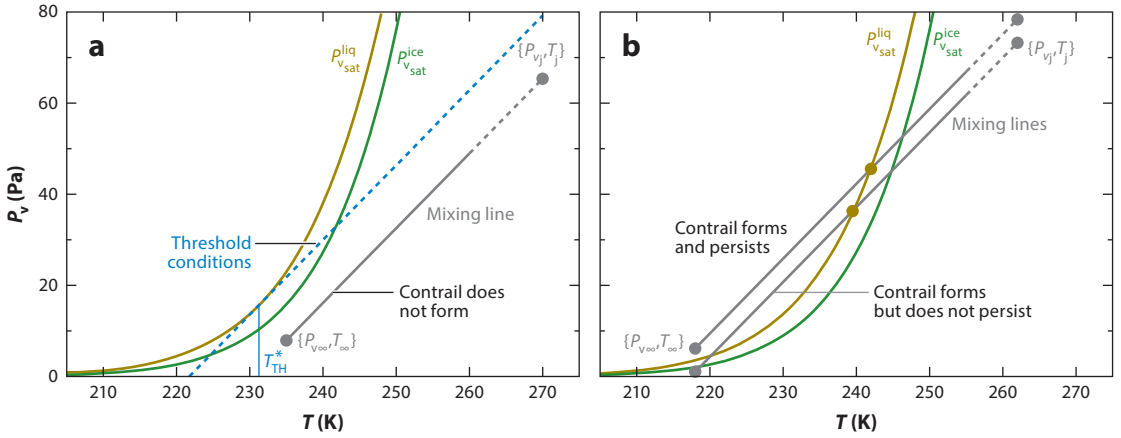

Figure 5

Three scenarios for condensation on the temperature–water vapor pressure diagram. The gray lines are the mixing lines, and each fluid element follows the path from exhaust (subscript j) to ambient (subscript ∞) conditions. Saturation curves with respect to water, $P^{liq}_{vsat}(T)$, and ice, $P^{ice}_{vsat}(T)$, are also represented. The conditions for contrail formation correspond to the point at which the mixing line first crosses the liquid saturation curve (Schumann 1996). In panel *a*, the threshold temperature T^*_{th} for the special case of 100% relative humidity is shown.

where EI_{H_2O} is the water vapor emission index (mass of vapor added by combustion per mass of fuel), $c_p = 1{,}004\,\mathrm{J\,Kg^{-1}\,K^{-1}}$ is the heat capacity of air (with its temperature dependence neglected), $\varepsilon \equiv 0.622 = W_{H_2O}/W_{air}$ is the vapor-to-air ratio of molar masses, and Q is the combustion heat per mass of fuel. The quantity η is the overall engine efficiency in cruise conditions, defined as the mechanical energy output of the engines (thrust $\times$ distance per mass of fuel) divided by Q. Therefore, $(1-\eta)Q$ represents the heat delivered to the exhaust.

The saturation curves for liquid water and ice, $P^{liq}_{vsat}(T)$ and $P^{ice}_{vsat}(T)$, can be derived from the Clausius-Clapeyron equilibrium equations for a perfect gas,

$$\frac{\mathrm{d}\ln P^{liq}_{vsat}}{\mathrm{d}T} = \frac{L_{liq}(T)}{RT^2} \quad \text{and} \quad \frac{\mathrm{d}\ln P^{ice}_{vsat}}{\mathrm{d}T} = \frac{L_{ice}(T)}{RT^2}, \tag{3}$$

where $L_{liq}(T)$ and $L_{ice}(T)$ are the latent heats of evaporation and sublimation, respectively, and $R = 8.31447\,\mathrm{J\,mol^{-1}\,K^{-1}}$ is the molar gas constant. The functional dependence of latent heats on temperature is quite complex (Pruppacher & Klett 1997), and approximations have been proposed in the literature with fitting parameters adapted to the temperature range of interest for contrails (Murphy & Koops 2005).

As a fluid element traverses the mixing line, it first reaches ice saturation and then liquid saturation. It is now believed that a necessary condition for contrail formation is the latter. This is indicated both by observations of the location at which a contrail becomes visible (e.g., Kärcher & Yu 2009, paragraph 8) and by studies of nucleation discussed in Section 2.3.

Schumann (1996) posed the following question. Suppose we know the slope G of the mixing line and the ambient vapor pressure (which fixes the horizontal line on which ambient conditions lie). Then we seek to determine the warmest (threshold) ambient temperature T_{th} at which contrails will form. For the threshold case, the mixing line will be tangent to the liquid saturation curve, and T_{th} can be determined from Schumann (1996, equation 11). For the special case of 100% relative humidity, which is the case depicted in **Figure 5*a***, T_{th} is determined by simply imposing the tangency condition $\mathrm{d}P^{liq}_{vsat}/\mathrm{d}T = G$.

The Schmidt-Appleman criterion determines only whether a contrail can form, and it does not discriminate between linear contrails that evaporate soon after formation and persistent contrails that evolve into cirrus. Persistency is possible only if the ambient air is supersaturated with respect to ice, $P_{v\infty} > P_{vsat}^{ice}(T_\infty)$. The Schmidt-Appleman criterion has been validated by in situ measurements (Busen & Schumann 1995, Schumann et al. 1996, Petzold et al. 1997, Jensen et al. 1998b) and numerical simulations (Paoli et al. 2004, 2013). Interestingly, Equation 2 implies that modern aircraft that have higher propulsion efficiency (and therefore cooler exhausts) may form contrails at ambient higher temperatures over a larger range of cruise altitudes, as nicely shown in experiments by Schumann et al. (2000).

2.2. Ice Growth

An ice crystal grows by the deposition of water vapor onto its surface at a rate proportional to the difference between the vapor pressure in the ambient and the vapor pressure just above its surface. The latter is the saturation vapor pressure over ice increased by Kelvin's curvature correction (which therefore reduces the deposition rate). Vapor is initially available from the exhausting jet and then by the entrainment of supersaturated ambient air. Following textbooks (Pruppacher & Klett 1997, Jacobson 1999), we can express the mass growth rate of a single crystal as

$$\frac{dm_p}{dt} = \frac{4\pi\, C_p D_v [P_v - P_{vsat}^{ice} \exp(a_{Kel}/\delta)]}{R_v T + L_s D_v P_{vsat}^{ice} [L_s/(R_v T) - 1]/(\mathcal{K} T)}. \quad (4)$$

The quantity C_p is the ice crystal capacitance and accounts for the solution to the steady diffusion equation for a nonspherical particle. Specifically, it replaces the particle radius for nonspherical particles. The quantities D_v and $\mathcal{K}$ are the vapor and thermal diffusion coefficients modified to account for ventilation effects (i.e., convective transport around the particle) and transition from the free molecular to the diffusion-limited growth regime, and L_s is the latent heat of sublimation. The factor $\exp(a_{Kel}/\delta)$ is Kelvin's curvature correction, where δ is the radius for a spherical particle and the length a_{Kel} involves the surface tension of the ice-vapor interface. Slightly different forms of Equation 4 have been published. Sometimes partial pressure is replaced by the vapor number density, $n_v \equiv X_v n$ (e.g., Kärcher 2003). Equation 4 has been modified to include radiative effects in the context of cirrus modeling (Sölch & Kärcher 2010), although they have not been reported to be significant for contrails.

The Nakaya crystal morphology diagram depicts the empirically observed shape (which Equation 4 cannot predict) that ice crystals assume with a given homogeneous temperature and supersaturation (Libbrecht 2005, 2012). Much has been learned in the past few years about how one could go about predicting the shape, and for this we refer the reader to the given references. Perhaps someday these ideas will be applied to contrails and cirrus clouds and will include ventilation (i.e., advective transport) effects.

2.3. Nucleation

For the numerator of Equation 4 to be greater than zero in supersaturated conditions, Kelvin's curvature correction requires a minimum initial particle size (which depends on the ambient humidity). The process by which this threshold is reached is called nucleation. To uncover the main elements of the nucleation process, studies carry out simulations using single-parcel models that incorporate as much of the known microphysics (e.g., coagulation) and chemistry as possible, while prescribing the overall mixing. Some early references are Kärcher et al. (1996), Kärcher (1998, 1999), and Fahey et al. (1999).

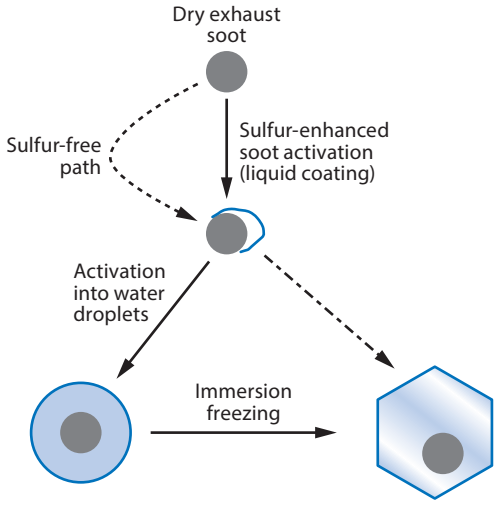

Figure 6

Schematic illustration of soot activation (Kärcher 1998, 1999). The solid/dashed arrows denote activation paths with/without sulfur. The sulfur-enhanced path is controlled by the adsorption of oxidized sulfur molecules and scavenging of H_2SO_4 and H_2O droplets. Activation into water droplets occurs when the plume $RH_w > 100\%$. Few ice particles nucleate below water saturation (*dotted-dashed arrow*). Figure adapted with permission from Kärcher (1999).

More recent works are Kärcher & Yu (2009) and Wong & Miake-Lye (2010). These authors concluded that nucleation by soot particles dominates for soot emission indices $EI_{soot} > 10^{14}$– 10^{15} particles per kilogram fuel, which includes the range of values for the current commercial fleet (Petzold et al. 1999). Soot particles become suitable nuclei after being activated by adsorbed H_2SO_4, SO_3, and H_2SO_4-H_2O (Wong & Miake-Lye 2010). They then scavenge (by coagulation) H_2O droplets; this is followed by immersion freezing. An ice nucleus is thus born. This pathway is illustrated in **Figure 6**. The effect of fuel sulfur content was found to be weak when varied over its current range in jet fuels, consistent with the early experiments of Busen & Schumann (1995). The chemi-ion-mediated nucleation scheme (Yu 2006) does produce more H_2SO_4-H_2O droplets, but they do not freeze because they are too acidic. One remaining unknown pointed out in the latter work is the role played by ultrafine droplets consisting of organics. The problem of nucleation of ice particles in contrails was recently revisited by Kärcher et al. (2015).

2.4. Particle Motion and Sedimentation

The equations for the position $\mathbf{X}(t)$ and speed $\mathbf{U}(t)$ of a particle are

$$\dot{\mathbf{X}} = \mathbf{U}, \tag{5}$$

$$m\dot{\mathbf{U}} = \mathbf{F}_D + mg, \tag{6}$$

where the drag force (for a sphere of radius a) is

$$\mathbf{F}_D = C_D(\mathrm{Re})\frac{1}{2}\rho_{air}|\mathbf{u}_{rel}|^2\pi a^2\hat{\mathbf{u}}_{rel}. \tag{7}$$

The quantity $\mathbf{u}_{rel} \equiv \mathbf{u}(\mathbf{X}) - \mathbf{U}$ is the gas velocity, $\mathbf{u}(\mathbf{X})$, relative to the particle; a hat denotes a unit vector; and $C_D(\mathrm{Re})$ is the drag coefficient as a function of the Reynolds number,

$\mathrm{Re} \equiv 2\rho_{\mathrm{air}}|\mathbf{u}_{\mathrm{rel}}|a/\mu$. For $\mathrm{Re} \ll 1$, which is most often the case and should be checked a posteriori, we have $C_{\mathrm{D}} = 24/\mathrm{Re}$, and Equation 7 becomes Stokes' formula,

$$\mathbf{F}_{\mathrm{D}} = 6\pi\mu a\,\mathbf{u}_{\mathrm{rel}}, \tag{8}$$

which we henceforth assume. Equation 6 then becomes

$$\dot{\mathbf{U}} = \tau_{\mathrm{D}}^{-1}(\mathbf{u} - \mathbf{U}) + \mathbf{g}, \tag{9}$$

where

$$\tau_{\mathrm{D}} = m/6\pi\mu a \tag{10}$$

is the timescale for drag to act. It is easy to computationally implement Equations 5 and 9 to track individual particles. However, τ_{D} is often much smaller than the timescale over which the gas velocity $\mathbf{u}$ changes following the particle (the local strain rate may be used to estimate this), and a prohibitively small time step is needed. In this case, an expansion in powers of τ_{D} (normalized by the flow time) can be performed following Haller & Sapsis (2008). The leading-order result for the particle velocity is

$$\mathbf{U} = \mathbf{u} + \tau_{\mathrm{D}}(\mathbf{g} - D\mathbf{u}/Dt) + \mathcal{O}(\tau_{\mathrm{D}}^2), \tag{11}$$

where the term $\tau_{\mathrm{D}}\mathbf{g}$ represents sedimentation in the gravitational field, and $-\tau_{\mathrm{D}}\,D\mathbf{u}/Dt$ represents sedimentation due to the fictitious (d'Alembert) force arising from gas acceleration. The second term, important for the effect discussed in the next paragraph, has not been included in the contrail literature to our knowledge.

Haller & Sapsis (2008) and Sapsis & Haller (2010) found that inertial particles have an attracting set. Their results imply that ice particles should tend to concentrate on a particular closed streamline surrounding each vortex (e.g., see figure 3 in Sapsis & Haller 2010 for the case of Hill's spherical vortex, which is analogous to a vortex pair). It would be of interest to study the extent to which the attractor is realized in contrails in the presence of turbulent exhaust and vortex instabilities. It would also be interesting to study whether the photograph of a hollow contrail presented by Unterstrasser (2014, p. 7551) is indicative of this process. If this process does occur, it may lead to the collision and coagulation of ice particles.

In the early phases, particles do not undergo significant gravitational sedimentation (see, e.g., Naiman et al. 2011, Unterstrasser 2014). In the diffusion phase, sedimentation becomes important and manifests in the form of fall streaks. Different crystal habits are formed in this phase. For studies of the terminal velocity of nonspherical particles, the reader is referred to Heymsfield & Iaquinta (2000), Khvorostyanov & Curry (2002), and Mitchell 77 & Heymsfield (2005).

2.5. Parameters for the Size and Shape of Ice Crystals

In the early phases of contrail evolution, ice crystals can be safely considered to be spherical particles (Schröder et al. 2000, p. 470; Gayet et al. 2012). This may result from the highly fluctuating environment to which they are exposed. At late times, sedimentation, wind shear, and other atmospheric effects lead to highly anisotropic habits. **Figure 7** shows a schematic illustration of typical habits encountered in contrails and cirrus, and Heymsfield et al. (2010, table 1) reviewed some in situ studies on crystal shapes in contrails.

For the purposes of microphysical and radiative transfer parameterization, there are a few key quantities that characterize the size and shape of a collection of particles. Each particle has a volume $\mathcal{V}(D_{\mathrm{p}})$ and projected area (cross section in a generic direction) $\mathcal{A}(D_{\mathrm{p}})$, where D_{p} is a characteristic size of the particle, typically the maximum dimension in the objects shown in the figure. [Common parameterizations in atmospheric modeling are $\mathcal{V}_{\mathrm{p}} = a\,D_{\mathrm{p}}^{b}$, $m_{\mathrm{p}} = \rho_{\mathrm{ice}}\mathcal{V}_{\mathrm{p}}$, and $\mathcal{A}_{\mathrm{p}} = \alpha\,D_{\mathrm{p}}^{\beta}$, where

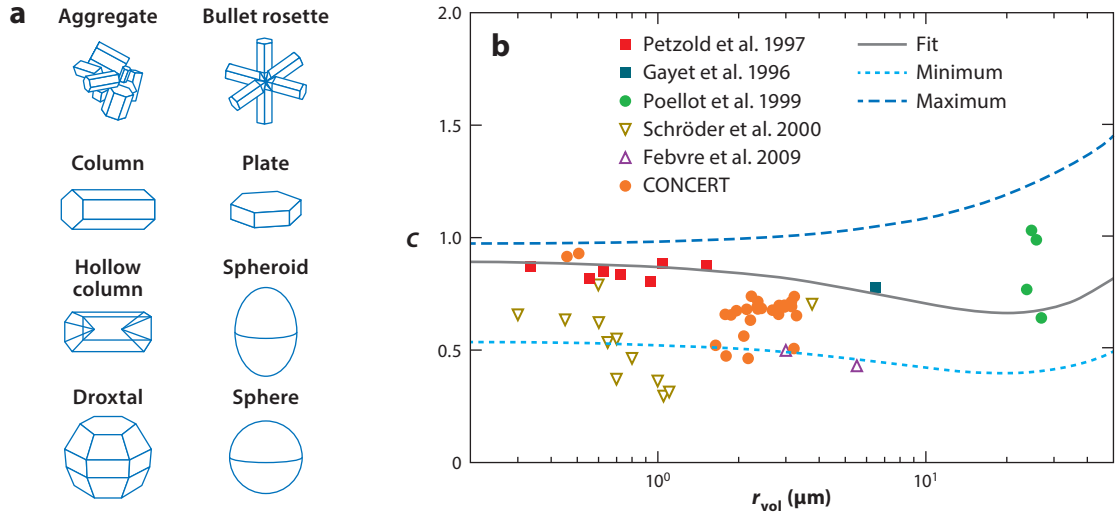

Figure 7

(*a*) Ice crystal habits in contrails and cirrus. Panel *a* adapted with permission from Yang et al. (2005). (*b*) The ratio $C \equiv r_{\text{vol}}/r_{\text{eff}}$, which is an important parameter for the contrail optical depth and depends on the size and shape distributions of the collection of ice particles. The data shown here are reconstructed from various observational campaigns. $r_{\text{eff}} \equiv 3V/4A$ and $r_{\text{vol}} = [3V/(4\pi N)]^{1/3}$, where V, A, and N are the total volume, surface area, and particle number, respectively, of the collection (see Equations 12 and 13). Note that $C = 1$ for monodisperse spherical crystals. Panel *b* adapted with permission from Schumann et al. (2011), © American Meteorological Society.

a, b, α, and β are parameters satisfying a specific habit, either analytically for simple geometries including spheres (for which $a = \pi/6$, $b = 3$, $\alpha = \pi/4$, and $\beta = 2$) via experimental fit.] For a collection of ice particles with random orientation, the number density, mean volume, and mean surface area are then given by

$$N = \int n(D)\,\mathrm{d}D, \quad V = \int \mathcal{V}(D)n(D)\,\mathrm{d}D, \quad \text{and} \quad A = \int \mathcal{A}(D)n(D)\,\mathrm{d}D, \tag{12}$$

where $n(D)$ is the particle size distribution. In microphysical and radiative transfer modeling, common quantities used to characterize the size and shape of particles in the collection are the effective radius r_{eff}, the volume radius r_{vol}, and the area radius r_{area} (Schumann et al. 2011):

$$r_{\text{eff}} = \frac{3V}{4A}, \quad r_{\text{vol}} = \left(\frac{3V}{4\pi N}\right)^{1/3}, \quad \text{and} \quad r_{\text{area}} = \left(\frac{A}{\pi N}\right)^{1/2}. \tag{13}$$

The ratio

$$C = \frac{r_{\text{vol}}}{r_{\text{eff}}} = \frac{r_{\text{area}}^2}{r_{\text{vol}}^2} \tag{14}$$

is related to the optical depth and is used in parameterizations.

2.6. Mathematical Modeling of Particle Transport

2.6.1. Lagrangian particle tracking. In the Lagrangian particle tracking (LPT) approach, a sample of ice particles is followed individually as they move in the fluid, and the tracking of their motion is described in Section 2.4. In LES, the fluid velocity is further decomposed into a grid-scale (filtered) velocity and a fluctuating velocity that depends on the local turbulent kinetic energy in the grid, otherwise known as subgrid kinetic energy (see, e.g., Sölch & Kärcher 2010, Naiman

LPT: Lagrangian particle tracking

et al. 2011). For purposes of removing vapor from the gas and supplying a drag force on the gas, each computational particle is assumed to represent a cluster of particles (Paoli et al. 2004, Sölch & Kärcher 2010, Unterstrasser & Sölch 2010). Sölch & Kärcher (2010) developed a complete contrail Lagrangian model that contains all microphysical processes (including nucleation, deposition, accretion, aggregation, sedimentation, and radiative transfer) that are relevant to contrail and cirrus physics.

2.6.2. Eulerian sectional approach. Eulerian sectional methods directly solve the transport equation for the particle size distribution in phase space $n(t, \mathbf{x}, \mathbf{U}, D)$ (see, e.g., Williams 1958, Hulburt & Katz 1964). In atmospheric applications, the effect of drag force is generally retained only to compute particle sedimentation, so that the particle velocity $\mathbf{U}$ is replaced by the sum of the fluid velocity $\mathbf{u}$ and the terminal velocity $u_T(D)$ (e.g., Ackerman et al. 1995, Hu & Srivastava 1995):

$$\frac{\partial n}{\partial t} + \nabla \cdot [(\mathbf{u} - u_T \hat{\mathbf{z}})\, n] + \frac{\partial (\dot{D} n)}{\partial D} = \omega, \tag{15}$$

where $\hat{\mathbf{z}}$ is the unit vector in the vertical direction, $\dot{D} \equiv dD/dt$ is the condensation/evaporation rate, and $\omega(t, \mathbf{x}, D)$ contains all sources and sinks for n, including nucleation, aggregation, collision/coalescence, and breakup. The fluid velocity $\mathbf{u}$ is further decomposed into mean and turbulent components. The term $\dot{D}$ is sometimes expressed in terms of the rate of change of the particle volume, $\dot{\mathcal{V}}(D) \equiv d\mathcal{V}(D)/dt$, or particle mass $\dot{m}(D) \equiv dm(D)/dt$ in phase space (e.g., Hu & Srivastava 1995). Equation 15 is discretized in N_{bin} sections or bins, $[D_i, D_{i+1}]$ with $i = 1, \ldots, N_{\text{bin}}$, and corresponding transport equations are evolved in physical space, which amounts to solving additional N_{bin} equations in each grid cell. Although the method retains the highest generality because it does not make any assumption on the form of n, it can be computationally expensive. For typical values of $N_{\text{bin}} = 50$–100, this leads to substantial CPU overhead, although techniques exist to optimize the operation of binning the size space (Lewellen et al. 2014).

2.6.3. Eulerian bulk approach. Eulerian bulk methods solve for the moments M_k of the size distribution,

$$M_k = \int_0^\infty D^k n(D) \mathrm{d}D, \tag{16}$$

by assuming a certain shape for $n(D)$ that depends on a limited number of parameters. Multiplying Equation 15 by D^k yields the transport equations for the moments (e.g., Paoli et al. 2002, Seifer & Beheng 2006, Ziemer et al. 2014):

$$\frac{\partial M_k}{\partial t} + \nabla \cdot (\mathbf{u} M_k) - \frac{\partial}{\partial z} \int_0^\infty u_T\, D^k n dD = \int_0^\infty D^{k-1} \dot{D} n dD + \int_0^\infty \omega D^k dD. \tag{17}$$

Commonly used shapes are the lognormal and gamma distributions for which Equation 16 can be solved analytically. Typically the zeroth (M_0) and third moment (M_3) are transported in contrail modeling (Spichtinger & Gierens 2009, Unterstrasser & Gierens 2010a, Paoli et al. 2012) as they can be related to the ice number density and ice water content:

$$\mathrm{IWC} = \int \rho_{\text{ice}} \mathcal{V}(D) n(D) \mathrm{d}D. \tag{18}$$

2.7. Radiative Transfer Essentials

A radiative transfer calculation is required not only as an a posteriori diagnostic to assess the RF induced by a contrail, but sometimes also during a calculation. For example, in cirrus clouds, there is radiation-induced convection and the suppression of sublimation by radiative cooling

(Dobbie & Jonas 2001). Radiative effects in contrails are discussed in Section 5. The governing equation is the radiative transfer equation (RTE) for the radiation intensity $I_\nu(\mathbf{x}, \hat{\mathbf{s}})$ (also called the spectral radiance) for each spatial location $\mathbf{x}$, frequency ν, and ray direction $\hat{\mathbf{s}}$. The RTE regards the medium as a continuum and expresses that $I_\nu(\mathbf{x}, \hat{\mathbf{s}})$ is conserved along each ray (a straight line along direction $\hat{\mathbf{s}}$), except for sinks and sources:

RTE: radiative transfer equation

ICA: independent column approximation

$$\nabla_{\mathbf{x}} \cdot [\hat{\mathbf{s}} I_\nu(\mathbf{x}, \hat{\mathbf{s}})] = \text{sinks and sources}. \tag{19}$$

It should be noted that the sinks and sources themselves depend on $I_\nu(\mathbf{x}, \hat{\mathbf{s}})$. Sinks include absorption and outscattering from the ray,

$$-(\eta_\nu^{\text{abs}} + \eta_\nu^{\text{sca}}) I_\nu(\mathbf{x}, \hat{\mathbf{s}}), \tag{20}$$

where η_ν^{abs} and η_ν^{sca} are coefficients with units of (length)$^{-1}$. The sum $\beta_\nu \equiv \eta_\nu^{\text{abs}} + \eta_\nu^{\text{sca}}$ is called the extinction coefficient, and the ratio $\eta_\nu^{\text{sca}} / (\eta_\nu^{\text{abs}} + \eta_\nu^{\text{sca}})$ is called the albedo. A nondimensional parameter, δ_ν, called the spectral optical depth, is often defined in place of distance along a ray:

$$\delta_\nu(s) = \int_0^s \beta_\nu(s)\, \mathrm{d}s. \tag{21}$$

If, along a given direction, $\delta_\nu(\ell) \ll 1$ when a region of length ℓ is traversed, then the region is said to be optically thin in that direction. If $\delta_\nu(\ell) \gg 1$, then the region is said to be optically thick.

Sources on the right-hand side of Equation 19 comprise emission by matter and scattering into direction $\hat{\mathbf{s}}$ from other directions. The scattering term is

$$\eta_\nu^{\text{sca}} \int_{\text{unit sphere}} I_\nu(\mathbf{x}, \hat{\mathbf{s}}') \phi(\hat{\mathbf{s}}, \hat{\mathbf{s}}') \mathrm{d}\Omega(\hat{\mathbf{s}}'), \tag{22}$$

where $\mathrm{d}\Omega(\hat{\mathbf{s}}')$ is a differential solid angle centered on $\hat{\mathbf{s}}'$, and the (normalized) function $\phi(\hat{\mathbf{s}}, \hat{\mathbf{s}}')$ is called the phase function. The scattering term couples different ray directions and makes the radiation problem particularly difficult. If local thermodynamic equilibrium holds between the matter and radiation, then the emission term is proportional to the Planck function $B_\nu(T)$. As fluid mechanicians, we can assume that absorption and scattering coefficients and the phase function are given. Specialists obtain them by solving a scattering problem in optics (Yang et al. 2005). In the single-scattering approximation, it is necessary to do this for each shape and size of ice crystal present and then combine the results assuming certain crystal size and shape distribution functions. For spherical particles, the optics problem has a classical exact solution due to Mie. Numerical methods suitable for solving the three-dimensional (3D) RTE when scattering is present include the discrete-ordinate method (e.g., Evans 1998) and Monte Carlo.

Once $I_\nu(\mathbf{x}, \hat{\mathbf{s}})$ is known, the radiative flux is obtained as

$$\mathbf{F}(\mathbf{x}) = \int \mathrm{d}\nu \int \hat{\mathbf{s}} I_\nu \, \mathrm{d}\Omega(\hat{\mathbf{s}}). \tag{23}$$

The gas energy equation requires $\nabla \cdot \mathbf{F}$, and by comparing Equations 19 and 23, one obtains

$$\nabla \cdot \mathbf{F} = \int \mathrm{d}\nu \int (\text{sinks and sources})\, \mathrm{d}\Omega(\hat{\mathbf{s}}), \tag{24}$$

which eliminates the need to compute a numerical divergence.

1D computations using the independent column approximation (ICA) (e.g., Fu & Liou 1993, Fu 1996, Fu et al. 1998, Morcrette et al. 1986, Morcrette 1991) are often performed instead of fully 3D radiative transfer calculations to reduce the computational burden, especially when they are coupled to 3D fluid flows. In this approximation, the assumption of local horizontal homogeneity is made in solving the RTE. For each vertical grid line, a plane parallel atmosphere is assumed. The radiation intensity is then a function of height z and angle θ relative to the vertical direction,

$I_\nu = I_\nu(z, \theta)$ (see, e.g., Modest 2003, p. 426). Solving the RTE for $I_\nu(z, \theta)$ requires integration in z together with a θ' integration at each z to account for scattering from θ' into θ. An upward integration is done to obtain I_ν for $0 \leq \theta < \pi/2$ and a downward integration for $\pi/2 < \theta \leq \pi$. Because of scattering between the up and down directions, these integrations generally must be iterated. Monte Carlo techniques have also been applied to the ICA (Barker et al. 2008). After $I_\nu(z, \theta)$ is known, upward and downward radiative fluxes, denoted $F^\uparrow$ and $F^\downarrow$, respectively, can be obtained from Equation 23. The radiative term in the gas energy equation is then

$$\left.\frac{\partial T}{\partial t}\right|_{\text{rad}} = \frac{1}{\rho c_{\text{p}}} \frac{\partial (F^\downarrow - F^\uparrow)}{\partial z}, \tag{25}$$

where $F^{\downarrow\uparrow}$ include the contributions from long-wave flux in the infrared band and the shortwave flux in the visible band. For idealized contrail simulations, the ICA compared well with the fully 3D calculations (particularly in the evaluation of radiative effects on contrail dynamics) with the largest differences occurring for low solar elevation angles (Gounou & Hogan 2007, Forster et al. 2012).

3D radiative transfer effects are of the same order of magnitude as the uncertainty in the parameterizations of optical properties (emissivity, optical depth, single-scattering albedo, and the asymmetry factor of the phase function) in both long-wave and shortwave radiation. Parameterizations of these quantities are provided by Ebert & Curry (1992) and Hong et al. (2009). The optical depth is of particular interest as it determines contrail visibility and enters into the parameterization of RF in global models (e.g., Meerkötter et al. 1999, Burkhardt & Kärcher 2011). It can be defined at each wavelength and is related to the extinction coefficient β by

$$\delta_\nu = \int_0^H \beta_\nu(z)\mathrm{d}z, \quad \text{with} \quad \beta_\nu = \int Q_{\text{ext}}(D, \lambda) A_{\text{p}}(D) n_{\text{p}}(D)\mathrm{d}D, \tag{26}$$

where H is the contrail vertical extension, and $Q_{\text{ext}}(D, \lambda)$ is the extinction efficiency, which depends on wavelength λ and particle size D. Using Equations 13 and 26, one can derive the relation between optical depth, mean particle size, and ice water path, $\text{IWP} \equiv \int_0^H \text{IWC}\ \mathrm{d}z$:

$$\langle \delta_\nu \rangle = \frac{3\langle Q_{\text{ext}} \rangle \text{IWP}}{4\rho_{\text{ice}} r_{\text{eff}}} = C \frac{3\langle Q_{\text{ext}} \rangle \text{IWP}}{4\rho_{\text{ice}} r_{\text{vol}}}, \tag{27}$$

where the angle brackets denote an average over a specified wavelength range (Schumann et al. 2011).

3. THE JET REGIME

According to the lifting-line picture (Batchelor 1967, p. 585), because of vorticity kinematics, spanwise variation in sectional circulation (proportional to sectional lift) necessitates a sheet of streamwise vorticity in the wake of the wing. At the wing tips, the change in sectional circulation is most abrupt; therefore, streamwise vorticity is strongest there. From a dynamical point of view, a spanwise pressure gradient along the wing leads to streamwise vorticity in the boundary layers of the wing. Similarly, at the wing tips, the pressure difference from the bottom to top surface of the wing causes a swirling motion. The sheet of streamwise vorticity eventually rolls up to form a pair of counter-rotating vortices. The tail, high-lift devices (if deployed), and wing-fuselage junction can also produce streamwise vorticity. During cruise, the roll-up generally completes over a distance of a few wingspans behind the aircraft, whereas during takeoff and landing, the wake rolls up into several corotating vortices that merge and form a single vortex farther downstream. This problem has been discussed in previous reviews (Spalart 1998, Rossow 1999, Gerz et al. 2002). In steady

(cruise) conditions, lift exactly balances the aircraft weight Mg, and the overall circulation Γ can be expressed as (Batchelor 1967, Jacquin et al. 2001, Gerz et al. 2002)

$$\Gamma = \frac{Mg}{\rho_\infty v_\infty b} \tag{28}$$

for an elliptically loaded wing, which is a good proxy for airplanes during cruise (Rossow 1999). Here ρ_∞, v_∞, and b are the free-stream density, aircraft speed, and vortex spacing, respectively. The vortex spacing is $b = \pi B/4$ in terms of wingspan B. The swirling velocity of each vortex is most often modeled using the Lamb-Oseen profile (Lamb 1932):

$$v_\theta(r) = \frac{\Gamma}{2\pi r}[1 - \exp(-r^2/a^2)], \tag{29}$$

where r is the distance from the vortex center, and $a = \sqrt{a_0^2 + 4\nu t}$ is the core size, with ν the kinematic viscosity of air. The initial core size a_0 can be obtained by matching the energy of the vortex pair to the energy of the elliptically loaded lifting line. Equation 29 is an exact laminar solution of the 2D axisymmetric Navier-Stokes equations (Batchelor 1967, p. 204) with a potential vortex behavior as $r \to \infty$. More refined models of trailing vortices include the axial velocity deficit arising from viscous decay (Batchelor 1964) or account for the transient roll-up of the vortex sheet (Moore & Saffman 1973). Saffman (1992) provided an excellent review of these models. A $v_\theta(r)$ profile fit to flight tests (P.R. Spalart, private communication) can be found in Shariff & Wray (2002, equation 2.5).

The interaction between the engine jet and trailing vortex has been characterized (Jacquin & Garnier 1996) using the ratio $\mathcal{R}$ of the excess axial momentum of the jet and the cross-flow momentum flux of the vortex across an area equal to that of the jet cross section $A(x) = \pi/4\, D^2(x)$ at a given downstream location x:

$$\mathcal{R}(x, r) = \frac{\rho_j v_j (v_j - v_\infty) A_j}{\rho_\infty v_\theta^2(r) A(x)}, \tag{30}$$

where r is the distance from the vortex center to the jet; and ρ_j, v_j, and A_j are the density, velocity, and cross-sectional area of the jet at the exit location, respectively. The value of $\mathcal{R}$ is initially high given the large jet momentum and then decreases downstream. Assuming $v_\theta \approx \Gamma/2\pi r$ and using jet expansion laws with correction for compressible flows (Pope 2000, Papamoschou & Roshko 1988), one can estimate the downstream location $x = x_j$ where the interaction starts by imposing $r = l_j$, the wing-tip-engine distance, and $\mathcal{R}(x, r_j) = 1$ in Equation 30 (Jacquin & Garnier 1996). For a typical four-engine large-transport aircraft (e.g., a Boeing 747), this gives $x_{j_1} \sim B$ and $x_{j_2} \sim 5B$ for the outboard and inboard jet, respectively (see **Figure 8**), whereas for a two-engine type aircraft (e.g., a Boeing 767), this gives $x_j \sim 5B$. The interaction between a jet and a well-formed wing-tip vortex has been examined using numerical simulations (Ferreira Gago et al. 2002, Paoli et al. 2003), experiments (Brunet et al. 1999, Margaris et al. 2008), and simplified analytical models (Miake-Lye et al. 1993, Garnier et al. 1997). The dynamics are characterized by entrainment of the jet into the vortex flow field.

The interaction between the jet and vortex leads to the formation of secondary azimuthal vortices (rings), which cause stretching and distortion of the interface between the jet and external flow, followed by relatively large-scale engulfment of vapor into the rotational region (**Figure 9**). The velocity induced by wing-tip vortices outside their cores is an irrotational strain, so their first-order effect is to distort the jet cross sections into ellipses. It is known that laboratory elliptic jets have more violent mixing and entrainment than do circular ones (Husain & Hussain 1991). In simulations of jet-vortex interactions (Garnier et al. 1997, Paoli et al. 2003), there is faster decay of the jet velocity and increased surface area of mixing between the hot jet and the

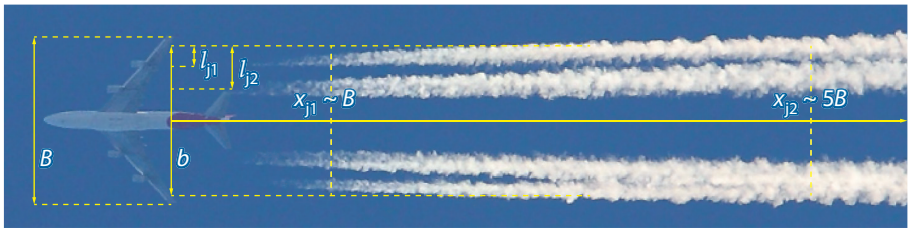

Figure 8

Photograph of jet/vortex interaction in a cruising four-engine aircraft, capturing the deflection of the exhaust jets by the trailing vortices and the downstream locations at which the interaction starts to be effective [$\mathcal{R}(x) = 1$ in Equation 30]: $x_{j1} \sim B$ and $x_{j2} \sim 5\,B$ for the outboard and inboard jets, respectively (Jacquin & Garnier 1996). Photograph taken from Wikipedia, copyright Fir0002/Flagstaffotos.

cold ambient air compared to the baseline coflowing jet. This affects the formation and early growth of ice crystals. Paoli et al. (2004) used LES coupled with LPT to study contrail formation in the first few seconds after jet emission and observed that ice crystals start to form at the edge of the jet where temperature is low and vapor is available for condensation (**Figure 10**). Enhanced mixing in the distorted jet favors the growth of ice crystals compared to the baseline case. This study was recently extended by Paoli et al. (2013), who analyzed contrail evolution up to 20 s in high supersaturated conditions for two- and four-engine model aircraft and for different number densities of soot particles. They observed that for a given amount of emitted water vapor, the total ice mass increases with the soot number density, but the mean crystal radius decreases because the same amount of vapor is shared among more particles. During the jet regime, the growth of ice crystals is maintained by the entrainment of humid ambient air, which overcomes the loss of available vapor by deposition. **Figure 11** shows that, because of vapor depletion, particles do not follow the mixing line but rather move toward the ice saturation curve, which is an indication of local thermodynamic equilibrium between ice and vapor phases.

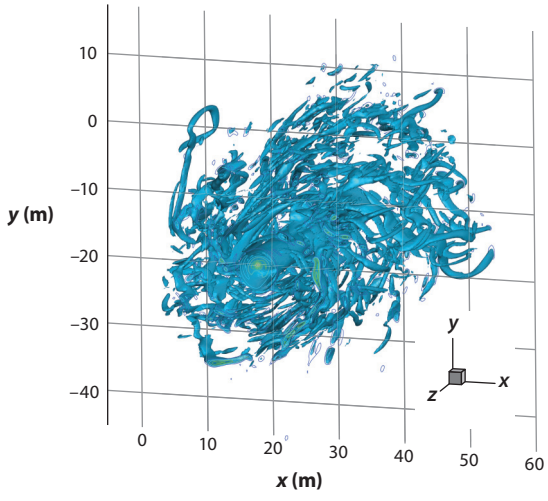

Figure 9

Results of a streamwise periodic simulation showing a snapshot of the vorticity magnitude. The trailing vortex is identified by the thick deformed tube in the center, which is surrounded by smaller vortex tubes that result from the interaction with the exhaust jet (Paoli et al. 2013).

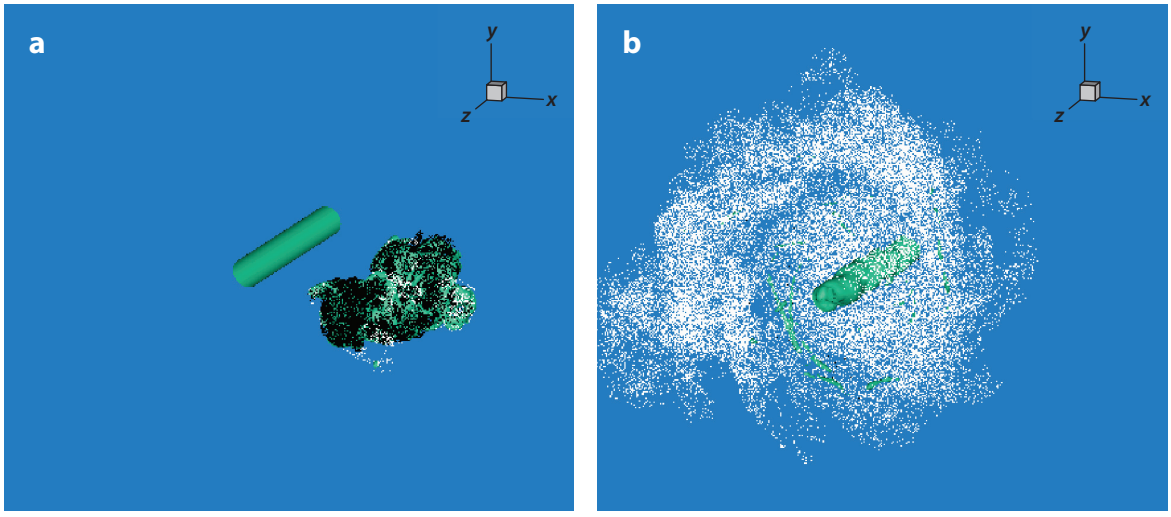

Figure 10

Results of a streamwise periodic simulation (Paoli et al. 2004) showing exhaust soot particles (*black dots*), ice crystals (*white dots*), and vorticity (*green isosurface*). Panel *a* shows the simulation at an early time, with the green column representing the wing-tip vortex.

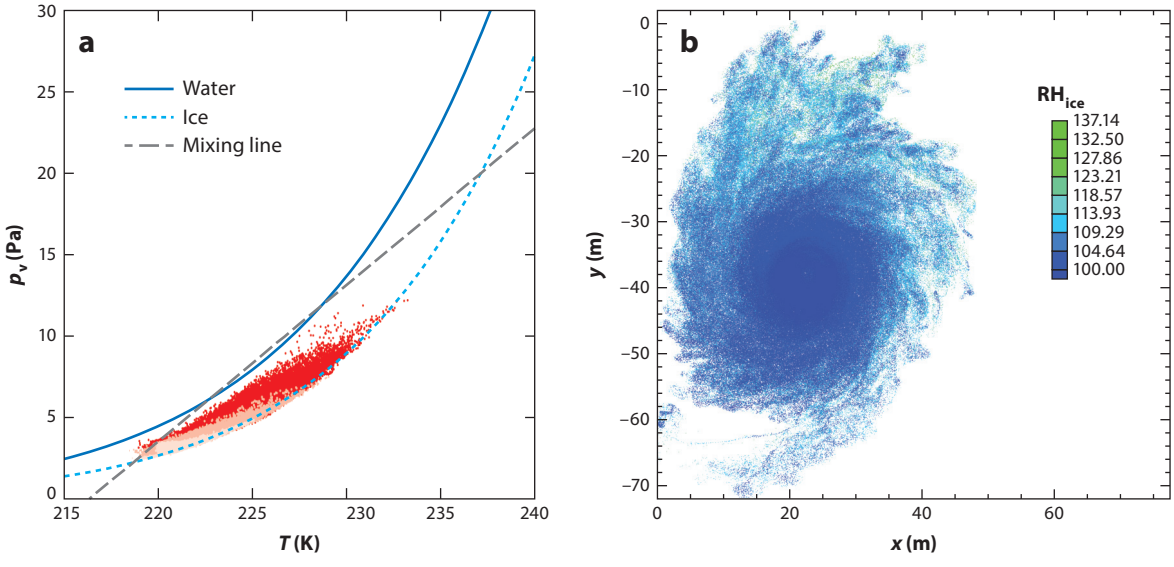

Figure 11

Results from the simulations of Paoli et al. (2013). (*a*) Particle scatter plots in the thermodynamic diagram $T - p_v$. Time increases from dark to light red. The saturation pressure with respect to water and ice is shown with solid dark blue and short-dashed light blue lines, respectively. The mixing line is shown with the long-dashed line. (*b*) Spatial particle distribution projected along the streamwise direction colored with the local RH_{ice}.

The studies referenced above employed simple ice microphysics integrated into solvers with fairly detailed fluid transport in the form of LES. Opposite to this are single-parcel models, which include tens of chemical species with detailed microphysics, but at the expense of a single trajectory in mixing space (e.g., Kärcher & Yu 2009, Wong & Miake-Lye 2010). A hybrid approach was presented by Paoli et al. (2008), who made complex particle microphysics calculations, taking as inputs a sample of many time histories extracted from temporal LES of the interaction between a vortex sheet and model jet.

4. VORTEX AND VORTICITY-DISSIPATION REGIMES

In a four-engine setup, the two distorted jets on each side of the aircraft eventually merge to form a single trail in which the ice particle density is (approximately) locally homogeneous in the axial direction and circumferentially around the vortex core. Thus begins the vortex phase, which lasts for a few minutes after emission. In this period, the contrail experiences important transformations in its vorticity structure, which influence the behavior of the ice phase. The vortex dynamics consist of two interacting aspects: the instability of the wing-tip vortices and the dynamics of stratification-induced secondary vorticity. The interaction depends on the Froude number, the initial disturbance amplitude, and vortex Reynolds number Γ/ν, the last two of which are ill-reproduced in simulations. A typical value for the Froude number, $\mathrm{Fr} \equiv \Gamma/2\pi\, b^2 N_{\mathrm{BV}}$, is $\approx$4, where N_{BV} is the Brunt-Väisälä frequency, defined below.

4.1. Vorticity Dynamics

Initially, the counter-rotating vortex pair descends at speed $v_{\mathrm{desc}} = \Gamma/2\pi b \sim 2\ \mathrm{ms}^{-1}$ and carries with it an oval-shaped volume of fluid. The oval is defined by the dividing streamline of vortex pair flow in a reference frame moving with the pair. The ambient atmosphere into which the oval descends is stratified with $P_0(z)$, $\rho_0(z)$, and $T_0(z)$ (pressure, density, and temperature, respectively) decreasing with height z. Because parcels of air moving vertically in the atmosphere generally experience adiabatic changes, what matters for residual buoyancy is the ambient gradient relative to the adiabatic value:

$$\frac{1}{T_0}\frac{\mathrm{d}T_0}{\mathrm{d}z} - \frac{\mathcal{R}}{c_{\mathrm{p}}}\frac{1}{P_0}\frac{\mathrm{d}P_0}{\mathrm{d}z} \equiv \frac{N_{\mathrm{BV}}^2}{g}. \tag{31}$$

Equation 31 defines the square N_{BV}^2 of the Brunt-Väisälä frequency. In a stably stratified atmosphere, we find that $N_{\mathrm{BV}}^2 > 0$. [The atmospheric community defines a potential temperature θ that is preserved in adiabatic changes: $\theta \equiv T/(P/P_{\mathrm{ref}})^{R/c_{\mathrm{p}}}$, where P_{ref} is a reference pressure. Equation 31 then becomes $\mathrm{d}\ln\theta_0/\mathrm{d}z = N_{\mathrm{BV}}^2/g$.] The value of N_{BV} is approximately $10^{-2}\ \mathrm{s}^{-1}$ at the tropopause and sharply increases to about twice this value as the stratosphere is entered (Pedlosky 1979).

The cores of wake vortices are prone to 3D instabilities that may be triggered by atmospheric or aircraft-induced turbulence. This has been extensively investigated mainly in the context of wake hazard (e.g., Spalart 1998, Jacquin et al. 2005). There is a long wavelength (equal to several vortex spacings) instability (Crow 1970) of the vortex tubes, which may coexist with a short wavelength (of the order of the vortex core size) instability (Widnall et al. 1974). Both instabilities are Kelvin (1880) modes of vortex bending that are amplified by the straining flow of the other vortex. It is interesting to ask whether even shorter Kelvin modes can be unstable. The critical Reynolds numbers of the Kelvin modes can be obtained (Shariff et al. 1994) by calibrating them to instability modes of homogeneous elliptic streamline flow (Bayly 1986, Landman & Saffman

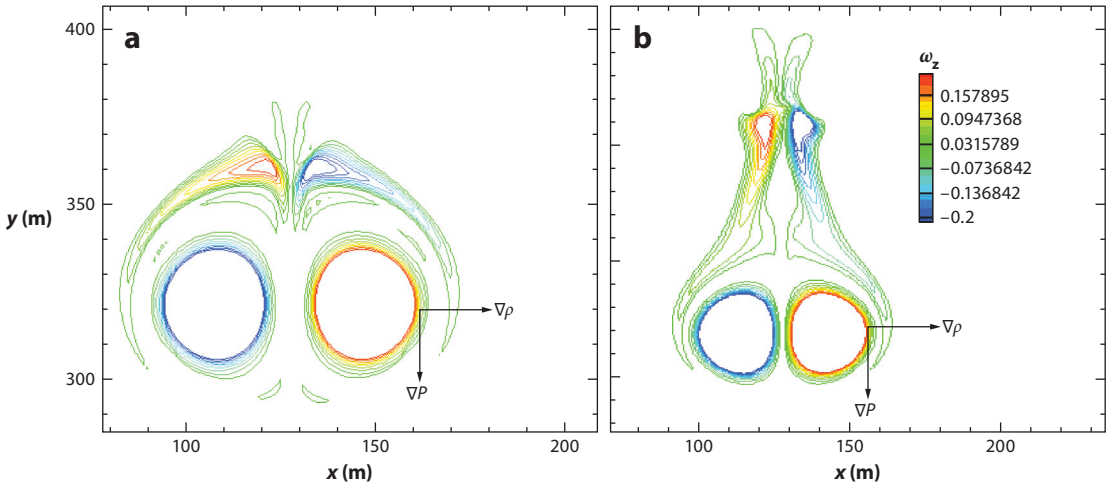

Figure 12

3D direct numerical simulation of a laminar vortex pair descending in a stratified atmosphere. Two wakes ages are represented. (*a*) Contours of axial vorticity show the formation, owing to baroclinic torque, of a layer of secondary vorticity. (*b*) Subsequent concentration of this vorticity forms an upward moving vortex pair, which is referred to as the secondary wake. Figure adapted from Paoli (2010).

1987). The conclusion is that higher modes are also unstable at flight Reynolds numbers. The effect of vortex core instabilities is to distort the oval-shaped interface and bring ambient fluid closer to the vortex cores.

Atmospheric stratification results in the production of buoyancy-induced vorticity at the boundary of the oval (Scorer & Davenport 1970). This vorticity is produced by a baroclinic torque term, as illustrated by the 2D vorticity transport equation,

$$\frac{D\omega}{Dt} = \frac{1}{\rho^2}\nabla\rho \times \nabla P, \tag{32}$$

which shows that the maximum production of vorticity occurs where the pressure and density gradients are perpendicular. The pressure gradient ∇P is dominated by the hydrostatic contribution (the contribution of advective acceleration is assumed to be negligible in comparison) and points vertically down, whereas $\nabla\rho$ is initially concentrated at the boundary of the oval and points outward from it (**Figure 12**). In each half of the wake, the secondary vorticity has a sign opposite to that of the primary vortices and eventually forms a counter-rotating vortex pair that moves upward, creating a secondary wake (Garten et al. 2001, Holzäpfel et al. 2001). Ice crystals can accumulate at the upper stagnation point, escape from the oval, and reach the flight level, forming a visible ice curtain that connects the primary and secondary wakes (Lewellen & Lewellen 2001, Unterstrasser & Gierens 2010a, Paugam et al. 2010, Naiman et al. 2011, Lewellen et al. 2014, Unterstrasser 2014). Because the secondary vorticity is of opposite sign, Rayleigh's criterion for centrifugal stability is violated. Using estimates of total growth, Shariff & Wray (2002) suggested that the secondary vorticity on the oval boundary can be susceptible to centrifugal instability. This assumes that the oval boundary remains intact.

The vortex pair spacing b is reduced because of the force of buoyancy (Spalart 1996). Turner's (1960) argument for this is that the impulse of a vortex pair is proportional to its spacing. Buoyancy reduces the impulse; therefore, the spacing must decrease at a rate that is easily written down. One consequence of the decrease in spacing is that fluid must be detrained from the shrinking

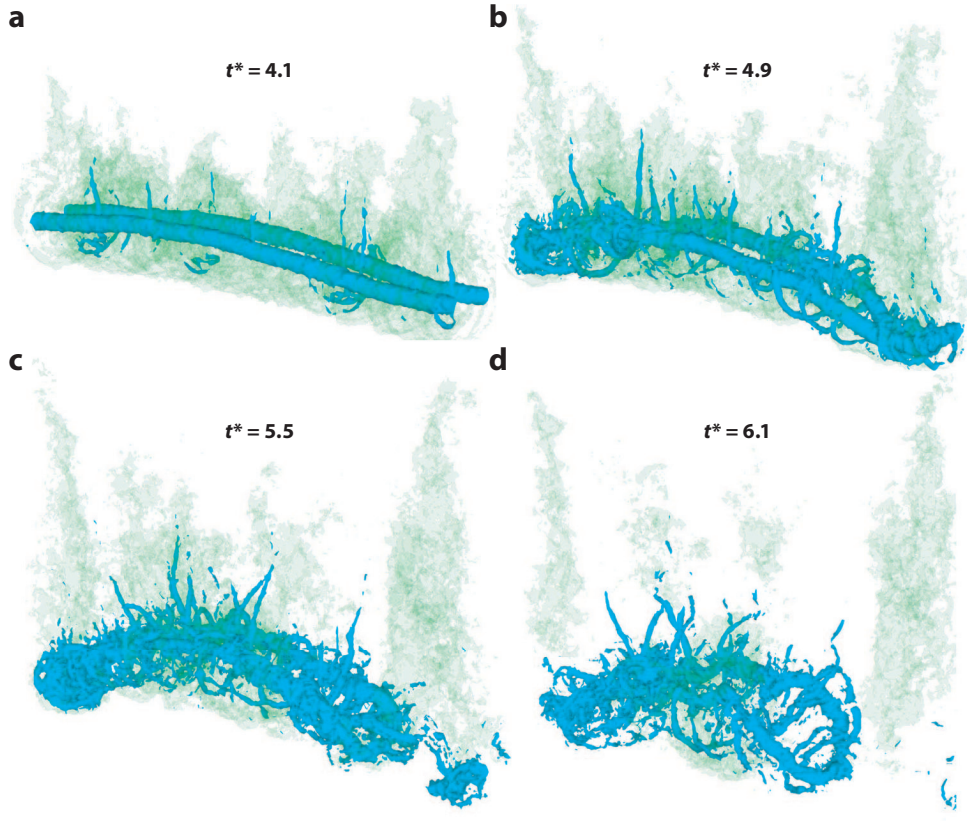

Figure 13

Perspective view of isosurfaces of the vorticity magnitude (*opaque blue*) and passive tracer (*transparent green*) at several vortex ages. Figure reproduced with permission from Misaka et al. (2012). Copyright 2012, AIP Publishing LLC.

oval. Another is that the mutually induced strain is enhanced, which accelerates the shortwave instability (Holzäpfel et al. 2001, Nomura et al. 2006). Eventually, at the end of this process, the vortex tubes collide and reconnect into distorted vortex rings.

4.2. Behavior of Ice Particles

The complex flow patterns described in the previous subsection are reflected in the properties of scalars (e.g., the vapor) and ice particles, trapped in and around the vortices. Recently, Misaka et al. (2012) examined in detail the dynamics and mixing of a passive scalar in a counter-rotating vortex pair (**Figure 13**). Unterstrasser et al. (2014) also analyzed the problem and found that atmospheric stratification, which is quantified by the Froude number, is the main parameter affecting the vertical extension of the wake.

Because of descent into higher pressure, the oval is compressed adiabatically (latent heat effects on wake dynamics are negligible), and its temperature rises at the adiabatic rate $-\mathrm{d}T_0/\mathrm{d}z = g/c_\mathrm{p} \sim 10\ \mathrm{K\ km^{-1}}$. A vertical displacement of 300 m leads to a 3-K increase, which may be sufficient to reduce supersaturation below zero and sublimate ice crystals. However, the large

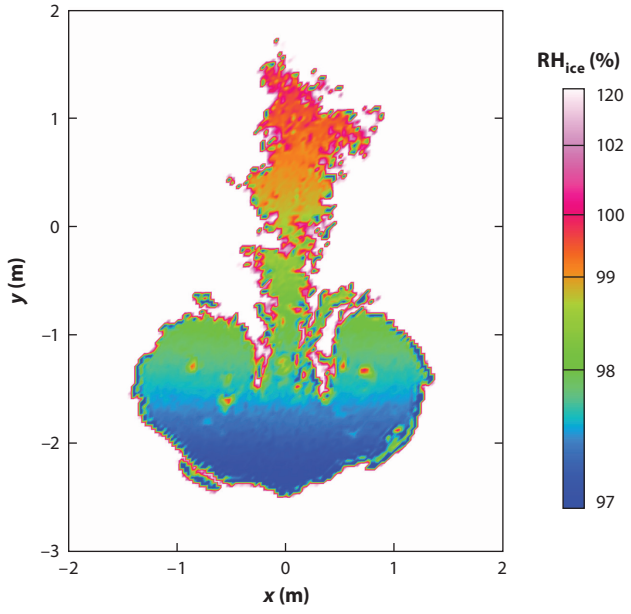

Figure 14

Results from the simulations of Naiman et al. (2011) illustrating a cross section of the contrail showing contours of relative humidity over ice. *x* is the horizontal and *y* the vertical direction. Figure adapted from Naiman et al. (2011), courtesy of A. Naiman.

amount of fresh vapor entrained into the oval ensures that conditions never get far from equilibrium (Sussmann & Gierens 2001, Naiman et al. 2011, Lewellen et al. 2014). This is demonstrated in **Figure 14**, which shows relative humidity over ice in the oval.

The fraction of ice crystals that sublimate depends on the ambient supersaturation and temperature (Unterstrasser & Gierens 2010a, Unterstrasser 2014) (see **Figure 15**). A fraction of ice crystals is not carried by the descending vortex because of the positive buoyancy of the hot exhaust jet (Gerz & Ehret 1997, Shirgaonkar & Lele 2007).

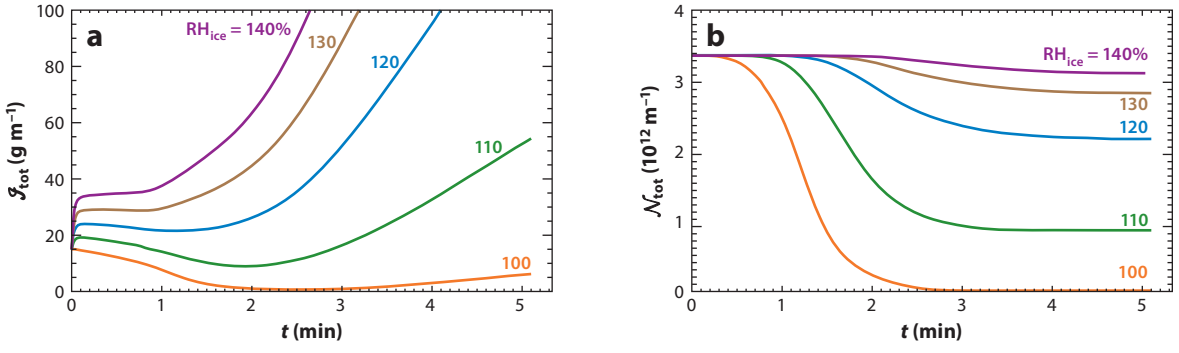

Figure 15

Results from the simulations of Unterstrasser (2014) showing the temporal evolution of ice crystal mass (*a*) and number (*b*) for ambient temperature $T_\infty = 217$ K and various ambient RH$_{ice}$. Figure adapted from Unterstrasser (2014), courtesy of S. Unterstrasser.

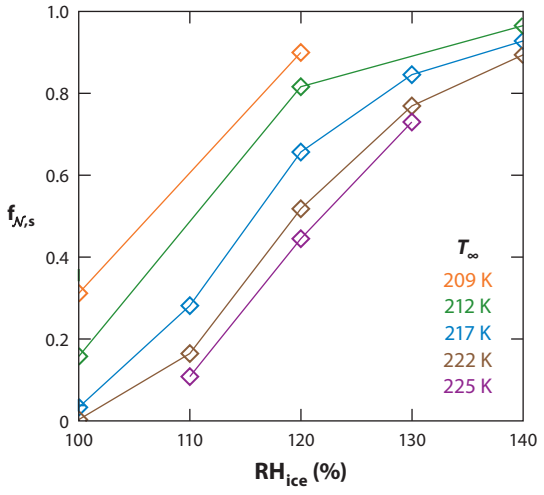

Figure 16

Results from the simulations of Unterstrasser (2014) illustrating the fraction of surviving ice crystal number at 5 min (the end of the vortex regime) as a function of ambient temperature and relative humidity. Figure adapted from Unterstrasser (2014), courtesy of S. Unterstrasser.

We now discuss LES studies of contrails in the vortex regime. A partial list of early studies includes Chlond (1998), Sussmann & Gierens (1999), Sussmann & Gierens (2001), and Lewellen & Lewellen (2001). These works have now been updated. The newer studies employ all the different kinds of approaches for modeling ice, namely 2D bulk microphysics (Unterstrasser et al. 2008), 2D LPT (Unterstrasser & Sölch 2010), 3D bulk microphysics (Paugam et al. 2010), 3D bin microphysics (Huebsch & Lewellen 2006, Lewellen et al. 2014), and 3D LPT (Naiman et al. 2011, Unterstrasser 2014, Picot et al. 2015). **Figure 15** shows the evolution of the total ice mass and fraction of surviving crystals in a sample of cases with fixed ambient temperature and various relative humidities (Unterstrasser 2014). The ice mass decreases because of ice sublimation in the primary wake; then it increases again at a rate that depends on RH_{ice}. The number of crystals decreases until it reaches a plateau. This behavior is consistent with other 3D LES in the vortex regime (Lewellen et al. 2014, Picot et al. 2015) and is generalized in **Figure 16** to varying ambient temperatures. For strongly saturated conditions, almost all ice crystals survive irrespective of temperature, whereas for moderately saturated and warm conditions, hardly any crystals survive the adiabatic temperature increase after 5 min (Unterstrasser & Sölch 2010, Unterstrasser 2014). **Figure 17** plots vertical profiles of these quantities. One can observe two peaks in the ice mass profile, identifying the primary and secondary wakes for $RH_i \geq 120$ % and sublimation occurring mostly in the primary wake for $RH_i \leq 110$ %. This is confirmed by the drift plots of the cross-stream integrated ice surface area in **Figure 18** (Lewellen et al. 2014).

In general, all these studies find that ambient humidity, stratification, and turbulence are the main factors controlling the survival of ice crystals, their mass, and spatial distribution at the end of the vortex regime. Turbulence affects the contrail characteristics in an indirect way by triggering Crow instability faster than in a calm atmosphere. For a given ambient turbulence, the descent distance increases with decreasing N_{BV}, which increases ice sublimation in the primary wake. For a given Brunt-Väisälä frequency, an increase in atmospheric turbulence leads to shorter decay, stronger mixing with ambient air, and a lesser vertical extent of the contrail. In the absence of turbulence, the primary wake falls deeper in the atmosphere, which results in lower ice

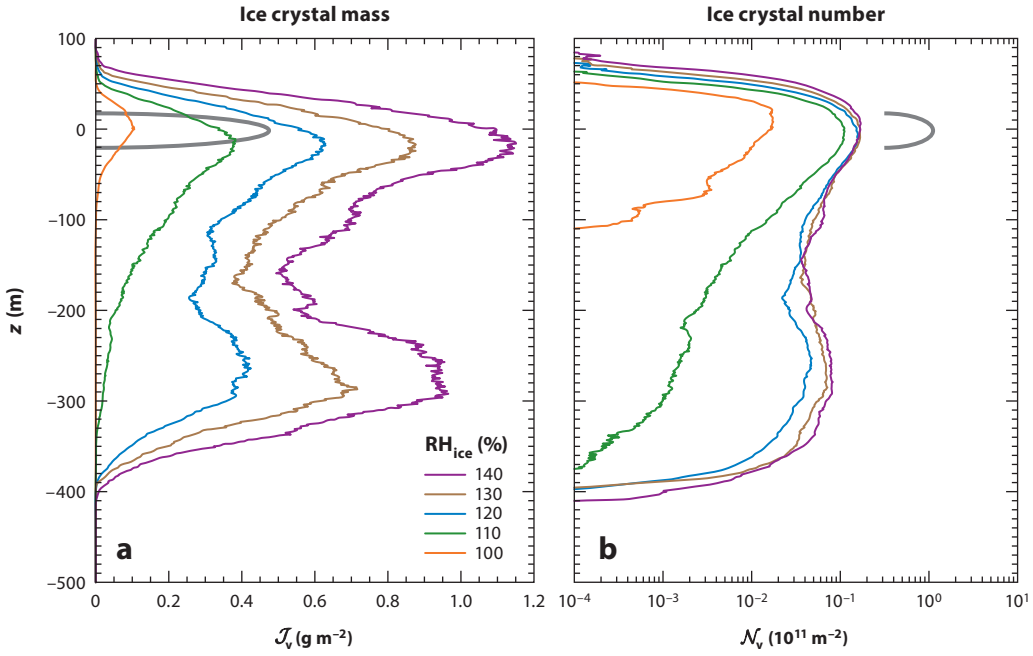

Figure 17

Results from the simulations of Unterstrasser (2014) showing simulated vertical profiles (at 5 min) of ice crystal mass (*a*) and number (*b*), integrated in the cross-stream direction and averaged in the axial direction. The ambient temperature is $T_\infty = 217$ K. The thick gray curves indicate the initial profiles. The different colors are coded for relative humidity, as in **Figure 15**. Figure adapted from Unterstrasser (2014), courtesy of S. Unterstrasser.

concentration in the secondary wake (Paugam et al. 2010). **Figure 19** shows an example of a 3D structure of ice mass for this case. One can observe that the largest ice crystals are located in the secondary wake at the top where the competition for available water vapor is lower because of the lower ice crystal concentration.

5. THE DIFFUSION REGIME

In the diffusion regime, which can last for several hours, the contrail spreads and transforms into cirrus, which persists if ambient conditions are supersaturated, until it sublimates by sedimenting into subsaturated layers or by entering into subsidence zones (Atlas et al. 2006). Contrail evolution in this phase is determined by ambient humidity, wind shear, atmospheric turbulence, and radiative effects. Sensitivity analyses based on 2D and 3D calculations have been recently published. They attempt to understand the intricate interactions between these effects and their role in determining the characteristics of the resulting contrail cirrus. For example, Unterstrasser & Gierens (2010a,b) employed 2D simulations, and Lewellen et al. (2014) and Lewellen (2014) performed 3D simulations with axially periodic boundary conditions. Both types of calculations should be interpreted as focusing on a certain axial width of the contrail and following its time development.

Ambient relative humidity and temperature were found to be the dominant parameters for contrail-to-cirrus transition. As expected, the total ice mass and total extinction increase as RH_{ice} increases (Unterstrasser & Gierens 2010a). **Figure 20** shows the long-term evolution of some

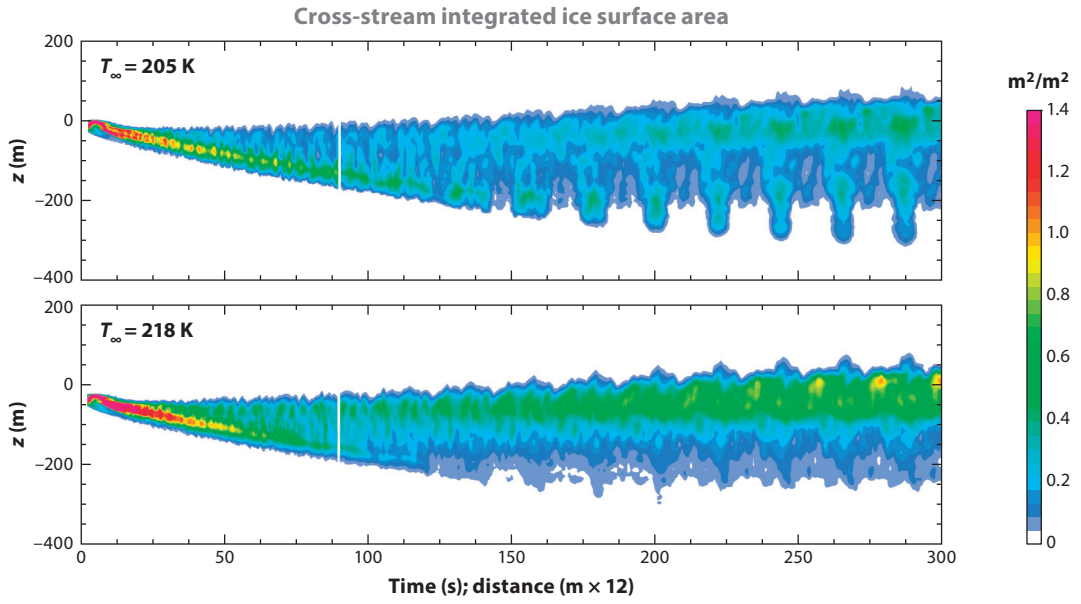

Figure 18

Drift plots from the simulations of Lewellen et al. (2014). The simulations are developing in time (axially periodic) with an axial domain size of 260 m (and ≈150 axial grid points) for most of the duration depicted. A drift plot is constructed by sampling data (as a function of time) on a cross-sectional plane of the simulation. Two cases are shown: $T_\infty = 205$ K (*top*) and $T_\infty = 218$ K (*bottom*). The tear drop structures in the upper figure result from downward-moving vortex loops created by vortex reconnection (Lewellen et al. 1998, figure 4). Figure adapted with permission from Lewellen et al. (2014), © American Meteorological Society.

of these quantities for a study involving a large number of cases (Lewellen 2014). Many of these results were obtained with quasi-3D simulations employing a few grid points in the axial direction.

Contrail spreading can be characterized by its cross-sectional area. One objective definition is the area where the extinction coefficient is above a threshold $\beta = 10^{-5}$ m^{-1} corresponding to lidar detection efficiency (Unterstrasser & Gierens 2010a). Wind shear increases horizontal contrail spreading (Gierens & Jensen 1998, Jensen et al. 1998a) and entrains fresh moist air in sufficiently high supersaturation conditions more effectively than atmospheric turbulent fluctuations. With fixed particle properties, a contrail becomes optically thinner when it is sheared (Naiman et al. 2011). However, shearing exposes the contrail to fresh humid air, which increases crystal size (Unterstrasser & Gierens 2010a) and optical thickness. Shear-induced optical thinning dominates at lower supersaturation, whereas size-induced optical thickening dominates at higher supersaturations.

Ice crystals begin to sediment when they reach sizes of tens of micrometers. Typically, the contrail cirrus will then exhibit a core region with a large concentration of relatively smaller particles and also fall streaks containing larger particles but in smaller quantities (**Figure 21**). The vertical flux of ice mass out of the contrail core can dehydrate the contrail core region (Unterstrasser & Gierens 2010a). The extent of the fall streak depends on the depth of the supersaturation layer where the contrail is immersed. We note from **Figure 20** that after a sufficiently long time, all crystals eventually sediment out and the contrail disappears. This time increases for lower temperatures.

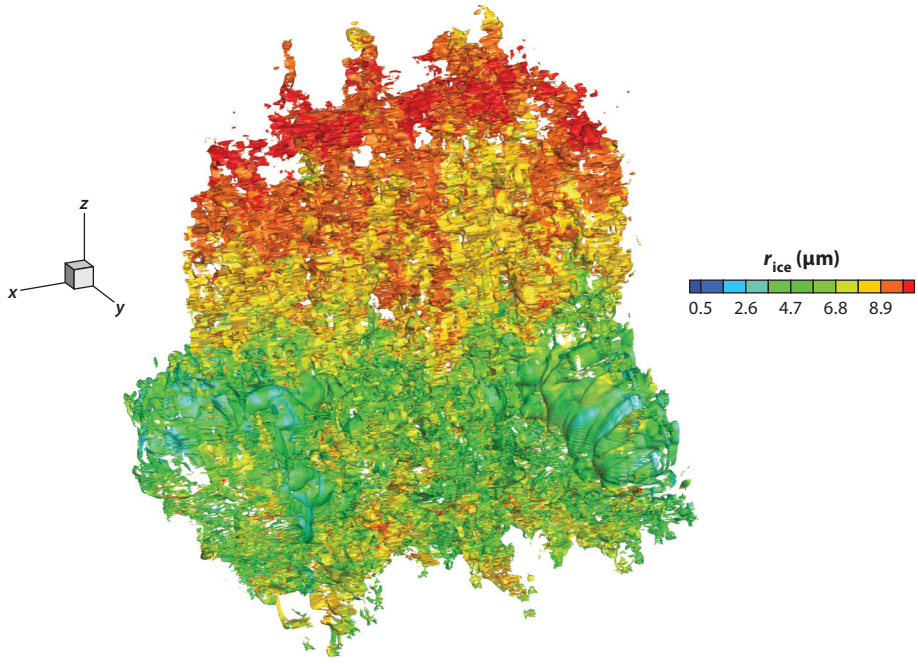

Figure 19

3D structure in the vortex regime 5 min after emission. The isosurface of the ice crystal mass density is colored with the ice crystal radius (Paugam et al. 2010). The secondary wake, which forms a curtain at the top, has larger sized crystals because of the availability of ambient vapor.

Predicting the contrail-to-cirrus transition requires a proper representation of atmospheric turbulence in the UTLS. Turbulent dispersion of passive scalars in the UTLS has been studied using simple analytical models (Konopka 1995) and numerical simulations, which provided estimates of turbulent diffusivities in the horizontal, vertical, and shear directions (Dürbeck & Gerz 1996, Gerz et al. 1998). In the aforementioned works and in the recent LES of contrails, atmospheric turbulence was not forced (Unterstrasser & Gierens 2010a) or was reinitialized after arbitrary time intervals (Lewellen et al. 2014, p. 4416). Because of the typically low Richardson numbers in the UTLS, atmospheric shear is not the primary source of fine-scale turbulence at these altitudes. Recently, following the review of Riley & Lelong (2000), there has been a resurgence of numerical simulations of stably stratified turbulence. These simulations employ low-wave-number stochastic forcing in spectral space (e.g., Brethouwer et al. 2007, Riley & Lindborg 2008, Waite 2011, Kimura & Herring 2012) or physical space (Paoli et al. 2014). These studies revealed the occurrence of large, elongated horizontal flow structures or pancakes. Ice crystals tend to distribute along these horizontal layers in the early diffusion regime when wake turbulence has dissipated and radiative effects are not yet effective (Paoli et al. 2012).

During the day, contrails are heated by infrared flux from below and visible flux from above. The resulting buoyancy lifts contrails to higher altitude and creates interior circulation (Unterstrasser & Gierens 2010b, Paoli et al. 2012, Lewellen 2014). Lift may prolong contrail lifetimes under conditions of high supersaturation and/or temperature (Unterstrasser & Gierens 2010b). Alternatively, Lewellen (2014) observed that the contrail lifetime is often reduced by radiative effects. He identified five regimes depending on ambient temperature and the blackbody radiation temperature of the Earth. For some combinations of these two parameters, the contrail

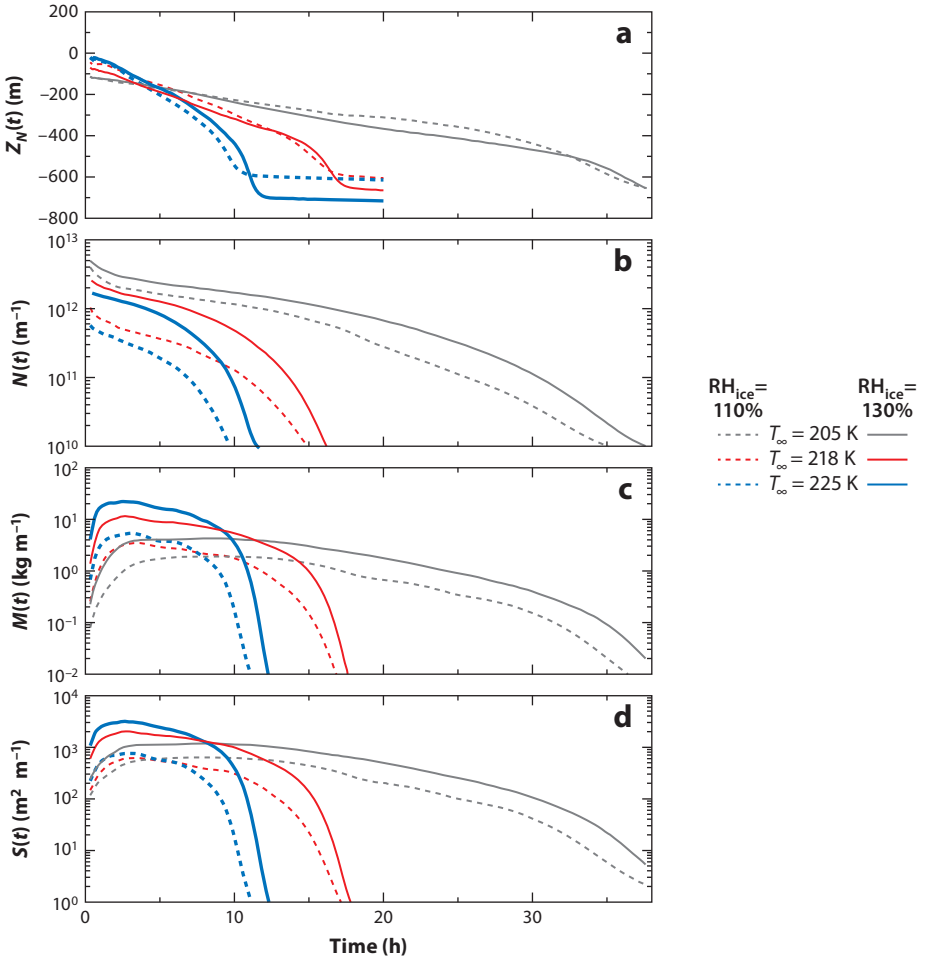

Figure 20

Simulation results of Lewellen (2014) for (*a*) the mean crystal altitude relative to the flight level, $Z_N(t)$; (*b*) crystal number per unit length, $N(t)$; (*c*) ice mass, $M(t)$; and (*d*) ice surface area, $S(t)$. The line types correspond to ambient temperature $T = 205$ K (*black*), 218 K (*red*), and 225 K (*green*) and ambient $RH_{ice} = 110\%$ (*dashed*) and 130% (*solid*). Figure adapted with permission from Lewellen (2014), © American Meteorological Society.

can actually cool. This, and the work of Schumann et al. (2012), demonstrates that one must include, in addition to contrail properties (optical depth, temperature, ice habits) and the 3D cloud structure, characteristics of the upwelling shortwave radiation, solar direct radiation, and outgoing long-wave radiation to capture the richness of radiative effects.

Simulations reported by Lewellen et al. (2014) show that the number of ice particles begins to decrease starting approximately 100 s after emission and reaches a power-law decay in time. This phenomenon, which is driven by the adiabatic heating during the vortex descent, is aided by the Kelvin curvature effect, which causes small particles to totally sublimate. At the same time, the total ice mass increases because the large particles continue to grow.

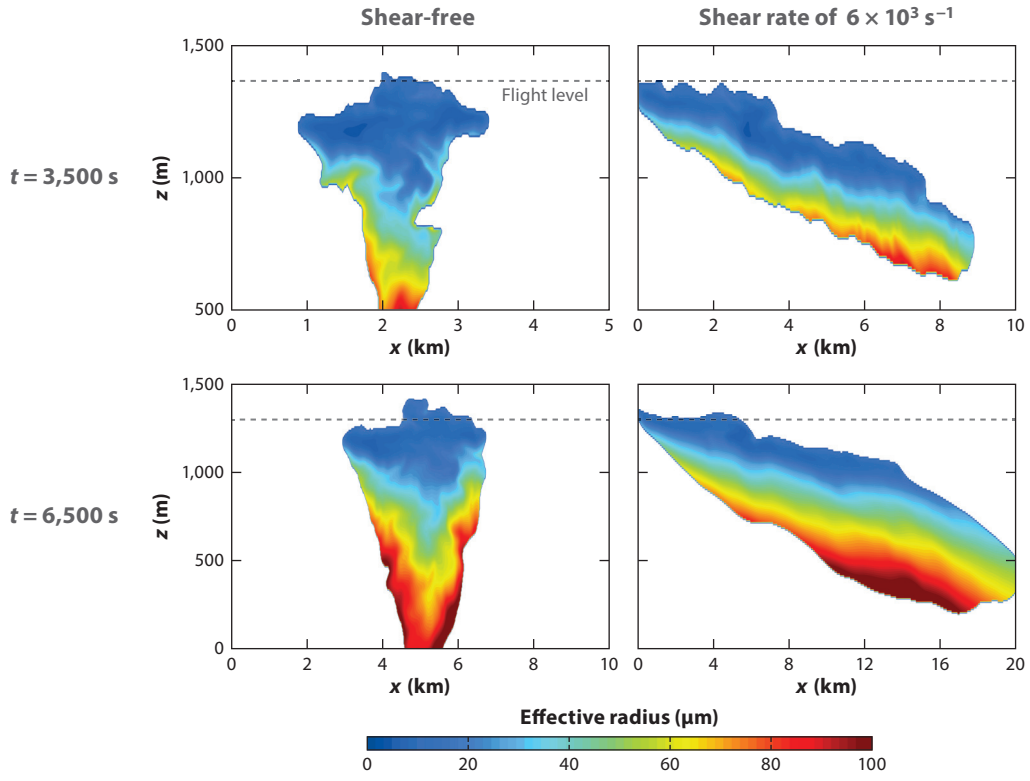

Figure 21

Simulation results of Unterstrasser & Gierens (2010b), who studied the effect of atmospheric shear on contrails.

6. DATA AVAILABLE FOR SIMULATION VALIDATION

Because of the difficulty of probing contrails in real flight conditions, the amount of experimental data available for model validation is in general scarce and difficult to exploit compared to situations in which controlled experiments can be performed. In situ measurements require dedicated and expensive flight campaigns, which are operationally challenging and potentially hazardous for the instrumented aircraft maneuvering in the wake of the contrail-generating aircraft, particularly in the jet and vortex regimes. Measurements were made in past campaigns by DLR (e.g., Petzold et al. 1997, 1999; Schröder et al. 2000) and by NASA in the framework of project SUCCESS (e.g., Spinhirne et al. 1998; see also Toon & Miake-Lye 1998, and references therein). These early studies also included satellite observations (Heymsfield et al. 1998, Minnis et al. 1998) and lidar measurements of contrails and cirrus (Freudenthaler et al. 1995, Sussmann 1999). Typical outputs are the peak particle and temperature concentration (to estimate dilution and indirectly the contrail width), ice water content, optical depth, and particle size distribution at various wake ages. These data have been used for broad validation (Sussmann & Gierens 2001, Paugam et al. 2010, Unterstrasser & Gierens 2010a, Paoli et al. 2013). Note that precise comparisons with simulations are cumbersome because it is impossible to exactly reproduce the same background of a particular experiment in the computational setup. Recently, the CONCERT campaign provided new measurement data from contrails generated by airlines along commercial routes (Voigt et al.

2010). In addition to the quantities listed above, these data include vertical profiles of particle concentration (Schumann et al. 2013) and cross-stream distributions of optical depth (Voigt et al. 2010). First comparisons with LES outputs are encouraging (Jessberger et al. 2013). For the very near field, it is obviously impossible to directly probe the contrail over the first few wingspans behind the aircraft; hence, one has to rely on laboratory studies that focus on measuring soot and volatile particle emissions (e.g., Petzold et al. 2003, Popovicheva et al. 2004, Wey et al. 2007, Wong et al. 2013). Finally, NASA has launched two large initiatives, ACCESS and ACCESS II, to study contrails generated using alternative fuels, particularly those with low or zero sulfur content.

SUMMARY POINTS

1. The RF of linear contrails, and more so due to contrail-induced cirrus, has a large uncertainty, which is a substantial fraction of the total aviation-induced forcing on the climate. The phenomenon also has aesthetic appeal because its myriad displays are often observed in the sky.
2. Given similarities in the governing physics, advances in contrail modeling and simulation will impact a major issue today, namely that of cloud forcing.
3. Contrail modeling involves a rich collection of physical and chemical principles and a wide range of length scales and timescales.
4. Great strides have recently been made to model and simulate contrails from "inception to demise" (Lewellen et al. 2014).
5. The role of high-fidelity simulations, whether purely hydrodynamic or coupled with microphysics and radiation, has been to reveal new phenomena and physical effects, model them, and evaluate their significance.
6. The literature shows that interactions between fluid mechanicians and atmospheric scientists have cross-fertilized new efforts by each.

FUTURE ISSUES

1. Fundamental fluid mechanical studies (theoretical, direct numerical simulation, and LES) are needed to understand turbulence structure and generation mechanisms in the UTLS.
2. At the high Reynolds numbers of aircraft wakes, instability mechanisms are theoretically possible that have not been observed in simulations, perhaps because they have much smaller Reynolds numbers or subgrid dissipation. One mechanism involves higher Kelvin modes in the vortex core (Section 4). Another involves centrifugal and Kelvin-Helmholtz instabilities in the baroclinically generated vortex oval surrounding the wake (Shariff & Wray 2002, p. 150). For the latter to grow, the oval boundary must remain intact.
3. What is the mechanism of the intriguing and often-observed mamma structures (Sussmann & Gierens 2001, figure 3)? Are they the same as the structures shown in **Figure 18**, which are the result of vortex loops formed after vortex reconnection?

4. Sapsis & Haller (2010) found that inertial particles in Hill's spherical vortex have an attracting set, which is a particular stream surface surrounding the vortex. The case of the vortex pair should be completely analogous. Is the photograph of a hollow contrail presented by Unterstrasser (2014, p. 7551) indicative of this effect? Is the convergence of ice particles toward the attractor sufficient to cause coagulation and local vapor starvation?
5. Zamansky et al. (2014) described a mechanism for turbulence generation by radiation. A small overdensity of particles collects more heat locally, leading to eddying motion, which, by the mechanism of preferential concentration, leads to a greater concentration of particles. Is this mechanism relevant to clouds or contrails?
6. Can current theories for the development of ice crystal morphology (e.g., Libbrecht 2012) be applied to contrails? Can ventilation (i.e., advective effects) be incorporated into these theories?
7. One can envision time-developing contrail calculations that use information (e.g., shear, updraft/downdraft, temperature, vapor content) from synoptic and mesoscale flow fields.
8. Time-developing dynamics (i.e., with axially periodic boundary conditions) are most often employed. The early jet regime is spatially developing. What effect does this have on the particle size distribution at the end of the jet regime?
9. Contrails have a wide variety of morphologies and histories. Citizen scientists can help in correlating different atmospheric conditions and aircraft types with different contrail structure on large and small scales. In this endeavor, they would combine their own observations together with publicly available data (e.g., vertical soundings and aircraft type) and more specialized data products that could be made available to them.
10. LES provide a large amount of data that cannot be integrated directly into global models. What is the relevant information that one should extract from these data, and how should one design parameterizations/subgrid-scale models that are compatible with the equations solved by the global model itself. A similar problem question has been considered in the case of aircraft gaseous emissions (Paoli et al. 2011). Another important point is how to optimize the choice of scenarios (atmospheric conditions, aircraft parameters) for the LES using systematic reduced-order modeling.
11. Because contrails, including short-lived nonpersistent ones, enhance aircraft visibility and detection, the study of ice nucleation, thermodynamics, and optics in the near-field wake is also relevant to military aviation.
12. In addition to the jet contrails discussed in this review, aerodynamic contrails have been recently investigated (Gierens et al. 2009, Kärcher et al. 2009, Gierens & Dilger 2013). They originate in the airflow over the wings instead of the exhaust air. They form in warmer air than jet contrails, and current understanding of their environmental impact remains poor.

DISCLOSURE STATEMENT

The authors are not aware of any biases that might be perceived as affecting the objectivity of this review.

ACKNOWLEDGMENTS

R.P. acknowledges financial support from DGAC (Direction Général de l'Aviation Civile) through project TC2 (Traînées de Condensation et Climat). R.P. wishes to thank Ulrike Burkhardt, Daniel Cariolle, François Garnier, Klaus Gierens, Bernd Kärcher, Sanjiva Lele, David Lewellen, Richard Miake-Lye, Ronan Paugam, Thierry Poinsot, Ulrich Schumann, Odile Thouron, Simon Unterstrasser, and Xavier Vancassel for the numerous, long-lasting, and vibrant discussions on various aspects of contrail physics and modeling.

LITERATURE CITED

Ackerman AS, Hobbs PV, Toon OB. 1995. A model for particle microphysics, turbulent mixing, and radiative transfer in the stratocumulus-topped marine boundary layer and comparisons with measurements. *J. Atmos. Sci.* 52:1204–36

Appleman H. 1953. The formation of exhaust condensation trails by jet aircraft. *Bull. Am. Meteorol. Soc.* 34:14–20

Atlas D, Wang Z, Duda DP. 2006. Contrails to cirrus—morphology, microphysics and radiative properties. *J. Appl. Meteorol. Climatol.* 45:5–19

Barker H, Cole J, Morcrette JJ, Pincus R, Räisänen P, et al. 2008. The Monte Carlo Independent Column Approximation: an assessment using several global atmospheric models. *Q. J. R. Meteorol. Soc.* 134:1463–78

Batchelor GK. 1964. Axial flow in trailing line vortices. *J. Fluid Mech.* 20:645–58

Batchelor GK. 1967. *An Introduction to Fluid Mechanics*. Cambridge, UK: Cambridge Univ. Press

Bayly BJ. 1986. Three-dimensional instability of elliptical flow. *Phys. Rev. Lett.* 57:2160–63

Brethouwer G, Billant P, Lindborg E, Chomaz JM. 2007. Scaling analysis and simulation of strongly stratified turbulent flows. *J. Fluid Mech.* 585:343–68

Brunet S, Garnier F, Jacquin L. 1999. *Numerical/experimental simulation of exhaust jet mixing in wake vortex*. Presented at AIAA Fluid Dyn. Conf., 30th, Norfolk, VA, AIAA Pap. 1999-3418

Burkhardt U, Kärcher B. 2009. Process-based simulation of contrail cirrus in a global climate model. *J. Geophys. Res.* 114:D16201

Burkhardt U, Kärcher B. 2011. Global radiative forcing from contrail cirrus. *Nat. Clim. Change* 1:54–58

Burkhardt U, Kärcher B, Schumann U. 2010. Global modeling of the contrail and contrail cirrus climate impact. *Bull. Am. Meteorol. Soc.* 91:479–84

Busen R, Schumann U. 1995. Visible contrail formation from fuels with different sulfur content. *Geophys. Res. Lett.* 22:1357–60

Cess RD, Potter GL, Blanchet JP, Boer GJ, Del Genio AD, et al. 1990. Intercomparison and interpretation of climate feedback processes in 19 atmospheric general circulation models. *J. Geophys. Res.* 95:16601–15

Chlond A. 1998. Large eddy simulation of contrails. *J. Atmos. Sci.* 55:796–819

Crow SC. 1970. Stability theory for a pair of trailing vortices. *AIAA J.* 8:2172–79

Dobbie S, Jonas P. 2001. Radiative influences on the structure and lifetimes of cirrus clouds. *Q. J. R. Meteorol. Soc.* 127:2663–82

Dürbeck T, Gerz T. 1996. Dispersion of aircraft exhausts in the free atmosphere. *J. Geophys. Res.* 101:26007–16

Ebert EE, Curry JA. 1992. A parameterization of ice cloud optical properties for climate models. *J. Geophys. Res.* 97:3831–36

Evans KF. 1998. The spherical harmonics discrete ordinate method for three-dimensional atmospheric radiative transfer. *J. Atmos. Sci.* 55:429–46

Fahey DW, Schumann U, Ackerman S, Artaxo P, Boucher O, et al. 1999. Aviation-produced aerosols and cloudiness. See Penner et al. 1999, pp. 65–120

Febvre G, Gayet J-F, Minikin A, Schlager H, Shcherbakov V, et al. 2009. On optical and microphysical characteristics of contrails and cirrus. *J. Geophys. Res.* 114:D02204

Ferreira Gago C, Brunet S, Garnier F. 2002. Numerical investigation of turbulent mixing in a jet/wake vortex interaction. *AIAA J.* 40:276–84

Forster L, Emde C, Unterstrasser S, Mayer B. 2012. Effects of three-dimensional photon transport on the radiative forcing of realistic contrails. *J. Atmos. Sci.* 69:2243–55

Freudenthaler V, Homburg F, Jäger H. 1995. Contrail observation by ground-based scanning lidar: cross-sectional growth. *Geophys. Res. Lett.* 22:3501–4

Fu Q. 1996. An accurate parameterization of the solar radiative properties of cirrus clouds for climate models. *J. Clim.* 9:2058–82

Fu Q, Liou KN. 1993. Parameterization of the radiative properties of cirrus clouds. *J. Atmos. Sci.* 50:2008–25

Fu Q, Yang P, Sun WB. 1998. An accurate parameterization of the infrared radiative properties of cirrus clouds for climate models. *J. Clim.* 11:2223–36

Fuglestvedt JS, Marquart S, Sausen R, Lee DS. 2003. Metrics of climatic change: assessing radiative forcing and emission indices. *Clim. Change* 58:267–331

Garnier F, Brunet S, Jacquin L. 1997. Modelling exhaust plume mixing in the near field of an aircraft. *Ann. Geophys.* 15:1468–77

Garten JF, Werne J, Fritts DC, Arendt S. 2001. Direct numerical simulation of the crow instability and subsequent vortex reconnection in a stratified fluid. *J. Fluid Mech.* 426:1–45

Gayet JF, Febvre G, Larsen H. 1996. The reliability of the PMS FSSP in the presence of small ice crystals. *J. Atmos. Ocean. Technol.* 13:1300–10

Gayet JF, Shcerbakov V, Voigt C, Schumann U, Schäuble D, et al. 2012. The evolution of microphysical and optical properties of an A380 contrail in the vortex phase. *Atmos. Chem. Phys.* 12:6629–43

Gerz T, Dürbeck T, Konopka P. 1998. Transport and effective diffusion of aircraft emissions. *J. Geophys. Res.* 103:25905–14

Gerz T, Ehret T. 1997. Wingtip vortices and exhaust jet during the jet regime of aircraft wakes. *Aerosp. Sci. Technol.* 1:463–74

Gerz T, Holzäpfel F, Darracq D. 2002. Commercial aircraft wake vortices. *Prog. Aerosp. Sci.* 38:181–208

Gierens K, Dilger F. 2013. A climatology of formation conditions for aerodynamic contrails. *Atmos. Chem. Phys.* 13:10847–57

Gierens K, Jensen E. 1998. A numerical study of the contrail-to-cirrus transition. *Geophys. Res. Lett.* 25:4341–44

Gierens K, Kärcher B, Mannstein H, Mayer B. 2009. Aerodynamic contrails: phenomenology and flow physics. *J. Atmos. Sci.* 66:217–26

Gierens K, Spichtinger P. 2000. On the size distribution of ice-supersaturated regions in the upper troposphere and lowermost stratosphere. *Ann. Geophys.* 18:499–504

Gounou A, Hogan RJ. 2007. A sensitivity study of the effect of horizontal photon transport on the radiative forcing of contrails. *J. Atmos. Sci.* 64:1706–16

Haller G, Sapsis T. 2008. Where do inertial particles go in fluid flows? *Physica D* 237:573–83

Heymsfield AJ, Baumgardner D, DeMott P, Forster P, Gierens K, Kärcher B. 2010. Contrail microphysics. *Bull. Am. Meteorol. Soc.* 91:465–72

Heymsfield AJ, Iaquinta J. 2000. Cirrus crystal terminal velocities. *J. Atmos Sci.* 57:916–38

Heymsfield AJ, Lawson RP, Sachse GW. 1998. Growth of ice crystals in a precipitating contrail. *Geophys. Res. Lett.* 25:1335–38

Holzäpfel F, Gerz T, Baumann R. 2001. The turbulent decay of trailing vortex pairs in stably stratified environments. *Aerosp. Sci. Technol.* 5:95–108

Hong G, Yang P, Baum BA, Heymsfield AJ, Xu KM. 2009. Parameterization of shortwave and longwave radiative properties of ice clouds for use in climate models. *J. Clim.* 22:6287–382

Hu Z, Srivastava RC. 1995. Evolution of raindrop size distribution by coalescence, breakup, and evaporation: theory and observations. *J. Atmos. Sci.* 52:1761–83

Huebsch WW, Lewellen DC. 2006. *Sensitivity study on contrail evolution*. Presented at AIAA Fluid Dyn. Conf. Exhib., 36th, San Francisco, AIAA Pap. 2006-3749

Hulburt HM, Katz S. 1964. Some problems in particle technology: a statistical mechanical formulation. *Chem. Eng. Sci.* 19:555–74

Husain H, Hussain F. 1991. Elliptic jets. Part 2. Dynamics of coherent structures: pairing. *J. Fluid Mech.* 233:439–82

Int. Civil Aviat. Organ. 2007. *ICAO environmental report 2007.* Rep., Int. Civil Aviat. Organ., Quebec. **http://www.icao.int/environmental-protection/Documents/Env_Report_07.pdf**

Jacobson MZ. 1999. *Fundamentals of Atmospheric Modeling*. Cambridge, UK: Cambridge Univ. Press

Jacobson MZ, Wilkerson JT, Naiman AD, Lele SK. 2011. The effects of aircraft on climate and pollution. Part I: Numerical methods for treating the subgrid evolution of discrete size- and composition-resolved contrails from all commercial flights worldwide. *J. Comput. Phys.* 230:5115–32

Jacquin L, Fabre D, Geoffroy P. 2001. *The properties of a transport aircraft wake in the extended near field: an experimental study*. Presented at AIAA Aerosp. Sci. Meet. Exhib., 39th, Reno, NV, AIAA Pap. 2001-1038

Jacquin L, Fabre D, Sipp D, Coustols E. 2005. Unsteadiness, instability and turbulence in trailing vortices. *C. R. Phys.* 6:399–414

Jacquin L, Garnier F. 1996. *On the dynamics of engine jets behind a transport aircraft*. Rep. AGARD CP-584, NATO, Brussels

Jensen EJ, Ackerman AS, Stevens DE, Toon OB, Minnis P. 1998a. Spreading and growth of contrails in a sheared environment. *J. Geophys. Res.* 103:31557–67

Jensen EJ, Toon OB, Kinnie S, Sachse GW, Anderson BE, et al. 1998b. Environmental conditions required for contrail formation and persistence. *J. Geophys. Res.* 103:3929–36

Jessberger P, Voigt C, Schumann U, Sölch I, Kaufmann S, et al. 2013. Aircraft type influence on contrail properties. *Atmos. Chem. Phys.* 38:11965–84

Kärcher B. 1998. Physicochemistry of aircraft-generated liquid aerosols, soot, and ice particles. 1. Model description. *J. Geophys. Res.* 103:17111–28

Kärcher B. 1999. Aviation-produced aerosols and contrails. *Surv. Geophys.* 20:113–67

Kärcher B. 2003. Simulating gas-aerosol-cirrus interactions: process-oriented microphysical model and applications. *Atmos. Chem. Phys.* 3:1645–64

Kärcher B, Burkhardt U, Bier A, Bock L, Ford IJ. 2015. The microphysical pathway to contrail formation. *J. Geophys. Res.* 120:7893–927

Kärcher B, Mayer B, Gierens K, Burkhardt U, Mannstein H. 2009. Aerodynamic contrails: microphysics and optical properties. *J. Atmos. Sci.* 66:227–43

Kärcher B, Peter T, Biermann UM, Schumann U. 1996. The initial composition of jet condensation trails. *J. Atmos. Sci.* 53:3066–82

Kärcher B, Yu F. 2009. Role of aircraft soot emissions in contrail formation. *Geophys. Res. Lett.* 36:L01804

Kelvin L. 1880. Vibrations of a columnar vortex. *Philos. Mag.* 10:155–68

Khvorostyanov V, Curry J. 2002. Terminal velocities of droplets and crystals: power laws with continuous parameters over the size spectrum. *J. Atmos. Sci.* 59:1872–84

Kimura Y, Herring JR. 2012. Energy spectra of stably stratified turbulence. *J. Fluid Mech.* 698:19–50

Konopka P. 1995. Analytical Gaussian solutions for anisotropic diffusion in a linear shear flow. *J. Non-Equilib. Thermodyn.* 20:78–91

Lamb H. 1932. *Hydrodynamics*. Cambridge, UK: Cambridge Univ. Press

Lamquin N, Stubenrauch CJ, Gierens K, Burkhardt U, Smit H. 2012. A global climatology of upper-tropospheric ice supersaturation occurrence inferred from the Atmospheric Infrared Sounder calibrated by MOZAIC. *Atmos. Chem. Phys.* 12:381–405

Landman MJ, Saffman PG. 1987. The three-dimensional instability of strained vortices in a viscous fluid. *Phys. Fluids* 30:2339–42

Lee DS, Fahey DW, Foster PM, Newton PJ, Wit RCN, et al. 2009. Aviation and global climate change in the 21th century. *Atmos. Environ.* 43:3520–37

Lee DS, Pitari G, Grewe V, Gierens K, Penner JE, et al. 2010. Transport impacts on atmosphere and climate: aviation. *Atmos. Environ.* 44:4678–743

Lewellen DC. 2014. Persistent contrails and contrail cirrus. Part II: Full lifetime behavior. *J. Atmos. Sci.* 71:4420–38

Lewellen DC, Lewellen WS. 2001. The effects of aircraft wake dynamics on contrail development. *J. Atmos. Sci.* 58:390–406

Lewellen DC, Lewellen WS, Poole L, DeCoursey R, Hansen G, et al. 1998. Large-eddy simulations and lidar measurements of vortex-pair breakup in aircraft wakes. *AIAA J.* 36:1439–45

Lewellen DC, Meza O, Huebsch WW. 2014. Persistent contrails and contrail cirrus. Part 1: Large-eddy simulations from inception to demise. *J. Atmos. Sci.* 71:4399–419

Libbrecht KG. 2005. The physics of snow crystals. *Rep. Prog. Phys.* 68:855–95

Libbrecht KG. 2012. Toward a comprehensive model of snow crystal growth dynamics: 1. Overarching features and physical origins. ArXiv:1211.5555 [cond-mat.mtrl-sci]
Margaris P, Marles D, Gursul I. 2008. Experiments on jet/vortex interaction. *Exp. Fluids* 44:261–78
Meerkötter R, Schumann U, Doelling DR, Minnis P, Nakajima T, Tsushima Y. 1999. Radiative forcing by contrails. *Ann. Geophys.* 17:1080–94
Miake-Lye RC, Martinez-Sanchez M, Brown RC, Kolb CE. 1993. Plume and wake dynamics, mixing and chemistry behind a high speed civil transport aircraft. *J. Aircr.* 30:467–79
Minnis P, Young DF, Garber DP, Nguyen L, Smith WL, Palikonda R. 1998. Transformation of contrails into cirrus during SUCCESS. *Geophys. Res. Lett.* 25:1157–60
Misaka T, Holzäpfel F, Hennemann I, Gerz T, Manhart M, Schwertfirm F. 2012. Vortex bursting and tracer transport of a counter-rotating vortex pair. *Phys. Fluids* 24:025104
Mitchell DL, Heymsfield AJ. 2005. Refinements in the treatment of ice particle terminal velocities, highlighting aggregates. *J. Atmos. Sci.* 62:1637–44
Modest MF. 2003. *Radiative Heat Transfer*. New York: Academic
Moore DW, Saffman PG. 1973. Axial flow in laminar trailing vortices. *Proc. R. Soc. Lond. A* 333:491–508
Morcrette JJ. 1991. Radiation and cloud radiative properties in the European Centre for Medium Range Weather Forecasts forecasting system. *J. Geophys. Res.* 96:9121–32
Morcrette JJ, Smith L, Fouquart Y. 1986. Pressure and temperature dependence of the absorption in longwave radiation parameterizations. *Beitr. Phys. Atmos.* 59:455–69
Murphy DM, Koops T. 2005. Review of the vapour pressures of ice and supercooled water for atmospheric applications. *Q. J. R. Meteorol. Soc.* 131:1539–65
Naiman AD, Lele SK, Jacobson MZ. 2011. Large eddy simulations of contrail development: sensitivity to initial and ambient conditions over first twenty minutes. *J. Geophys. Res.* 116:D21208
Nomura KK, Tsutsui H, Mahoney D, Rottman JW. 2006. Short-wavelength instability and decay of a vortex pair in a stratified fluid. *J. Fluid Mech.* 553:283–322
Paoli R. 2010. *Modeling and simulation of the environmental impact of aircraft emissions*. Habilitation Diss., Inst. Natl. Polytech. Toulouse
Paoli R, Cariolle D, Sausen R. 2011. Review of effective emissions modeling and computation. *Geosci. Model Dev.* 4:643–77
Paoli R, Hélie J, Poinsot T. 2004. Contrail formation in aircraft wakes. *J. Fluid Mech.* 502:361–73
Paoli R, Hélie J, Poinsot T, Ghosal S. 2002. Contrail formation in aircraft wakes using large-eddy simulations. In *Cent. Turbul. Res. Proc. Summer Prog. 2002*, pp. 229–41. Stanford, CA: Stanford Univ.
Paoli R, Laporte F, Cuenot B, Poinsot T. 2003. Dynamics and mixing in jet/vortex interactions. *Phys. Fluids* 15:1843–60
Paoli R, Nybelen L, Picot J, Cariolle D. 2013. Effects of jet/vortex interaction on contrail formation in supersaturated conditions. *Phys. Fluids* 25:053305
Paoli R, Thouron O, Escobar J, Picot J, Cariolle D. 2014. High-resolution large-eddy simulations of sub-kilometer-scale turbulence in the upper troposphere lower stratosphere. *Atmos. Chem. Phys.* 14: 5037–55
Paoli R, Thouron O, Picot J, Cariolle D. 2012. *Large-eddy simulations of contrail-to-cirrus transition in atmospheric turbulence.* Presented at Annu. Meet. Div. Fluid Dyn., Am. Phys. Soc., 65th, San Diego, CA
Paoli R, Vancassel X, Garnier F, Mirabel P. 2008. Large-eddy simulation of a turbulent jet and a vortex sheet interaction: particle formation and evolution in the near-field of an aircraft wake. *Meteorol. Z.* 17: 131–44
Papamoschou D, Roshko A. 1988. The compressible turbulent shear layer: an experimental study. *J. Fluid Mech.* 197:453–77
Paugam R, Paoli R, Cariolle D. 2010. Influence of vortex dynamics and atmospheric turbulence on the early evolution of a contrail. *Atmos. Chem. Phys.* 10:3933–52
Pedlosky J. 1979. *Geophysical Fluid Dynamics*. New York: Springer-Verlag
Penner JE, Lister DH, Griggs DJ, Dokken DJ, McFarland M, eds. 1999. *Aviation and the Global Atmosphere: A Special Report of the Intergovernmental Panel on Climate Change*. Cambridge, UK: Cambridge Univ. Press
Petzold A, Busen R, Schröder FP, Bauman R, Kuhn M, et al. 1997. Near field measurements on contrail properties from fuels with different sulfur content. *J. Geophys. Res.* 102:29867–81

Petzold A, Döpelheurer A, Brock CA, Schröder FP. 1999. In situ observations and model calculations of black carbon emission by aircraft at cruise altitude. *J. Geophys. Res.* 104:22171–81
Petzold A, Stein C, Nyeki S, Gysel M, Weingartner E, et al. 2003. Properties of jet engine combustion particles during the PartEmis experiment: microphysics and chemistry. *Geophys. Res. Lett.* 30:1719
Picot J, Paoli R, Thouron O, Cariolle D. 2015. Large-eddy simulation of contrail evolution in the vortex phase and its interaction with atmospheric turbulence. *Atmos. Chem. Phys.* 15:7369–89
Poellot M, Arnott W, Hallett J. 1999. In situ observations of contrail microphysics and implications for their radiative impact. *J. Geophys. Res.* 104:12077–84
Pope SB. 2000. *Turbulent Flows*. Cambridge, UK: Cambridge Univ. Press
Popovicheva OB, Persiantseva NM, Lukhovitskaya EE, Shonija NK, Zubareva NA, et al. 2004. Aircraft engine soot as contrail nuclei. *Geophys. Res. Lett.* 31:L11104
Prather M, Sausen R, Grossmann AS, Haywood JM, Rind D, Subbaraya BH. 1999. Potential climate change from aviation. See Penner et al. 1999, pp. 185–215
Pruppacher HR, Klett JD. 1997. *Microphysics of Clouds and Precipitation*. Dordrecht: Kluwer Acad.
Riese M, Ploeger F, Rap A, Vogel B, Konopka P, et al. 2012. Impact of uncertainties in atmospheric mixing on simulated UTLS composition and related radiative effects. *J. Geophys. Res. Atmos.* 117:D16305
Riley JJ, Lelong MP. 2000. Fluid motions in the presence of strong stable stratification. *Annu. Rev. Fluid Mech.* 32:613–57
Riley JJ, Lindborg E. 2008. Stratified turbulence: a possible interpretation of some geophysical turbulence measurements. *J. Atmos. Sci.* 65:2416–24
Rossow VJ. 1999. Lift-generated vortex wakes of subsonic transport aircraft. *Prog. Aerosp. Sci.* 35:507–660
Saffman PG. 1992. *Vortex Dynamics*. Cambridge, UK: Cambridge Univ. Press
Sapsis T, Haller G. 2010. Clustering criterion for inertial particles in two-dimensional time-periodic and three-dimensional steady flows. *Chaos* 20:017515
Sausen R, Isaksen I, Grewe V, Hauglustaine D, Lee DS, et al. 2005. Aviation radiative forcing in 2000: an update on IPCC. *Meteorol. Z.* 14:555–61
Schmidt E. 1941. Die Entstehung von Eisnebel aus den Auspuffgasen von Flugmotoren. In *Schriften der Deutschen Akademie der Luftfahrtforschung*, Vol. 44, pp. 1–15. Berlin: Verlag R. Oldenbourg
Schröder F, Kärcher B, Duroure C, Ström J, Petzold A, et al. 2000. On the transition of contrails into cirrus clouds. *J. Atmos. Sci.* 57:464–80
Schumann U. 1996. On conditions for contrail formation from aircraft exhausts. *Meteorol. Z.* 5:4–23
Schumann U. 2005. Formation, properties and climatic effects of contrails. *C. R. Phys.* 6:549–65
Schumann U. 2012. A contrail cirrus prediction model. *Geosci. Model Dev.* 5:543–80
Schumann U, Busen R, Plohr M. 2000. Experimental test of the influence of propulsion efficiency on contrail formation. *J. Aircr.* 37:1083–87
Schumann U, Jessberger P, Voigt C. 2013. Contrail ice particles in aircraft wakes and their climatic importance. *Geophys. Res. Lett.* 40:2867–72
Schumann U, Mayer B, Gierens K, Unterstrasser S, Jessberger P, et al. 2011. Effective radius of ice particles in cirrus and contrails. *J. Atmos. Sci.* 68:300–21
Schumann U, Mayer B, Graf K, Mannstein H. 2012. A parametric radiative forcing model for contrail cirrus. *J. Appl. Meteorol. Climatol.* 51:1391–406
Schumann U, Ström J, Busen R, Baumann R, Gierens K, et al. 1996. In situ observations of particles in jet aircraft exhausts and contrails for different sulfur containing fuels. *J. Geophys. Res.* 101:6853–69
Scorer RS, Davenport LJ. 1970. Contrail and aircraft downwash. *J. Fluid Mech.* 43:451–64
Seifert A, Beheng KD. 2006. A two-moment cloud microphysics parameterization for mixed-phase clouds. Part 1: Model description. *Meteorol. Z.* 92:45–66
Shariff K, Verzicco R, Orlandi P. 1994. A numerical study of three-dimensional vortex ring instabilities: viscous corrections and early nonlinear stage. *J. Fluid Mech.* 279:351–75
Shariff K, Wray A. 2002. Analysis of the radar reflectivity of aircraft vortex wakes. *J. Fluid Mech.* 463:121–61
Shine KP, Derwent RG, Wuebbles DJ, Mocrette JJ. 1990. Radiative forcing of climate. In *Climate Change: The IPCC Scientific Assessment*, ed. JT Houghton, GJ Jenkins, JJ Ephramus, pp. 41–68. Cambridge, UK: Cambridge Univ. Press

Shirgaonkar AA, Lele SK. 2007. Interaction of vortex wakes and buoyant jets: a study of two-dimensional dynamics. *Phys. Fluids* 19:086601
Sölch I, Kärcher B. 2010. A large-eddy model for cirrus clouds with explicit aerosol and ice microphysics and Lagrangian ice particle tracking. *Q. J. R. Meteorol. Soc.* 136:2074–93
Spalart PR. 1996. On the motion of laminar wing wakes in a stratified fluid. *J. Fluid Mech.* 327:139–60
Spalart PR. 1998. Airplane trailing vortices. *Annu. Rev. Fluid Mech.* 30:107–48
Spichtinger P, Gierens KM. 2009. Modelling of cirrus clouds—Part 1a: model description and validation. *Atmos. Chem. Phys.* 9:685–706
Spinhirne JD, Hart WD, Duda DP. 1998. Evolution of the morphology and microphysics of contrail cirrus from airborne remote sensing. *Geophys. Res. Lett.* 25:1153–56
Sussmann R. 1999. Vertical dispersion of an aircraft wake: aerosol-lidar analysis of entrainment and detrainment in the vortex regime. *J. Geophys. Res.* 104:2117–29
Sussmann R, Gierens K. 1999. Lidar and numerical studies on the different evolution of vortex pair and secondary wake in young contrails. *J. Geophys. Res.* 104:2131–42
Sussmann R, Gierens K. 2001. Differences in early contrail evolution of two-engine versus four-engine aircraft: lidar measurements and numerical simulations. *J. Geophys. Res.* 106:4899–911
Toon OB, Miake-Lye RC. 1998. Subsonic Aircraft: Contrail and Cloud Effects Special Study (SUCCESS). *Geophys. Res. Lett.* 25:1109–12
Turner JS. 1960. A comparison between buoyant vortex rings and pairs. *J. Fluid Mech.* 7:419–32
Unterstrasser S. 2014. Large-eddy simulation study of contrail microphysics and geometry during the vortex phase and consequences on contrail-to-cirrus transition. *J. Geophys. Res.* 119:7537–55
Unterstrasser S, Gierens K. 2010a. Numerical simulations of contrail-to-cirrus transition—Part 1: an extensive parametric study. *Atmos. Chem. Phys.* 10:2017–36
Unterstrasser S, Gierens K. 2010b. Numerical simulations of contrail-to-cirrus transition—Part 2: impact of initial ice crystal number, radiation, stratification, secondary nucleation and layer depth. *Atmos. Chem. Phys.* 10:2037–51
Unterstrasser S, Gierens K, Spichtinger P. 2008. The evolution of contrail microphysics in the vortex regime. *Meteorol. Z.* 17:145–56
Unterstrasser S, Paoli R, Sölch I, Kühnlein C, Gerz T. 2014. Dimension of aircraft exhaust plumes at cruise conditions: effect of wake vortices. *Atmos. Chem. Phys.* 14:2713–33
Unterstrasser S, Sölch I. 2010. Study of contrail microphysics in the vortex phase with a Lagrangian particle tracking model. *Atmos. Chem. Phys.* 10:10003–15
Voigt C, Schumann U, Jurkat T, Schäuble D, Schlager H, et al. 2010. In-situ observations of young contrails overview and selected results from the concert campaign. *Atmos. Chem. Phys.* 10:9039–56
Waite ML. 2011. Stratified turbulence at the buoyancy scale. *Phys. Fluids* 23:066602
Wey CC, Anderson BE, Wey C, Miake-Lye RC, Whitefield P, Howard R. 2007. Overview on the aircraft particle emissions experiment. *J. Propul. Power* 23:898–905
Widnall SE, Bliss D, Tsai CY. 1974. The instability of short waves on a vortex ring. *J. Fluid Mech.* 66: 35–47
Wilkerson JT, Jacobson MZ, Malwitz A, Balasubramanian S, Wayson R, et al. 2010. Analysis of emission data from global commercial aviation: 2004 and 2006. *Atmos. Chem. Phys.* 10:6391–408
Williams FA. 1958. Spray combustion and atomization. *Phys. Fluids* 1:541–45
Wong HW, Beyersdorf AJ, Heath CM, Ziemba LD, Winstead EL, et al. 2013. Laboratory and modeling studies on the effects of water and soot emissions and ambient conditions on the properties of contrail ice particles in the jet regime. *Atmos. Chem. Phys.* 13:10049–60
Wong HW, Miake-Lye RC. 2010. Parametric studies of contrail ice particle formation in jet regime using microphysical parcel modeling. *Atmos. Chem. Phys.* 10:3261–72
Yang P, Hong G, Dessler AE, Ou SSC, Liou KN, et al. 2010. Contrails and induced cirrus: optics and radiation. *Bull. Am. Meteorol. Soc.* 91:473–78
Yang P, Wei H, Huang HL, Baum BA, Hu YX, et al. 2005. Scattering and absorption property database for nonspherical ice particles in the near- through far-infrared spectral region. *Appl. Opt.* 44:5512–23

Yu F. 2006. From molecular clusters to nanoparticles: second-generation ion-mediated nucleation model. *Atmos. Chem. Phys.* 6:5193–211

Zamansky R, Coletti F, Massot M, Mani A. 2014. Radiation induces turbulence in particle-laden fluids. *Phys. Fluids* 26:071701

Ziemer C, Jasor G, Wacker U, Beheng KD, Polifke W. 2014. Quantitative comparison of presumed-number-density and quadrature moment methods for the parameterisation of drop sedimentation. *Meteorol. Z.* 41:411–23